Studying the extreme Universe through gamma-ray emitting Active Galactic Nuclei

Yéssica Calatayud Borràs

Supervisors:
Josefa Becerra & Mireia Nievas

Master's Final project

Master in Astrophysics

Universidad de La Laguna

July 2024

Resumen

Los rayos gamma son producidos por los fenómenos más extremos del Universo. Constituyen la radiación más energética del espectro electromagnético, con $E > 100\,KeV$. La atmósfera terrestre absorbe la mayoría de estas radiaciones, por lo que los rayos gamma solo pueden ser detectados directamente desde el espacio. En tierra, se utilizan grandes áreas colectoras para detectar estos rayos gamma mediante la radiación Cherenkov emitida por las cascadas de partículas que generan en la atmósfera. A energías por debajo de 100 GeV, las imágenes resultantes de las cascadas son pequeñas y difíciles de distinguir de las causadas por rayos cósmicos.

Existen diferentes procesos de emisión de rayos gamma, como la dispersión Compton inversa, la radiación sincrotrón, la radiación de curvatura, el bremsstrahlung y la desintegración de piones neutros. La absorción de rayos gamma puede ocurrir por dispersión de Compton o producción de pares electrón-positrón. Estos rayos se detectan en diversos objetos celestes, tanto galácticos como extragalácticos.

Los núcleos activos de galaxias (AGNs) son importantes emisores de rayos gamma y se pueden clasificar según su orientación y características espectrales. Los blazares, AGNs con los jets orientados en dirección a la Tierra, presentan variabilidad rápida y mayor Doppler boosting. Se dividen en: BL Lacertae (BLL) y Flat Spectrum Radio Quasar (FSRQ). Estos están caracterizados por su distribución espectral de energía (SED) con dos picos, el primero atribuido a emisión sincrotrón y el segundo, puede deberse a procesos hadrónicos o leptónicos. Otros ejemplos de AGNs son las radio galaxias y las galaxias Seyfert.

El telescopio espacial *Fermi*, con su instrumento LAT, ha sido crucial para comprender la física detrás de los jets relativistas que emergen de los agujeros negros supermasivos en los centros de AGNs. Este trabajo realizó un estudio de 96 AGNs detectados por *Fermi*-LAT durante 14 años de observaciones. Se utilizaron los datos de su índice fotónico (índice espectral de la ley de potencias que describe el segundo pico de la SED en el rango de rayos gamma) proporcionado por el catálogo 4FGL-DR2 de *Fermi*-LAT y sus curvas de luz proporcionadas por su repositorio de curvas de luz (LCR).

Los objetivos de este estudio incluyeron: a) realizar un análisis temporal de las fuentes y la identificación de llamaradas ('flares') en la banda de energía de 0.1 a 100 GeV; b) estudiar la relación entre los tipos de AGN y el comportamiento del índice espectral durante las llamaradas; c) realizar un estudio sistemático de toda la muestra y, adicionalmente, un análisis individual de las fuentes con características destacadas; d) utilizar estos resultados para identificar fuentes interesantes para observar con telescopios Cherenkov. En este trabajo se propusieron y compararon dos definiciones de flare estadísticas: el primero es un criterio de umbral basado en el flujo promedio durante períodos de aumento de flujo, y el segundo es un análisis de Bloques Bayesianos. También se emplearon métodos estadísticos para definir la duración de los flares (larga, media, corta) según la longitud total de la curva de luz actual de las fuentes y cuándo una fuente se define como brillante.

Los resultados encontrados más importantes y su interpretación física son los siguientes:

- De las 96 fuentes, 46 mostraron al menos un flare largo, 31 al menos uno corto y 12 mostraron ambas, indicando que diferentes regiones o procesos de emisión dentro de los jets podrían ser responsables de los flares de diferentes duraciones. Flares cortos y medianos pueden ayudar a restringir los parámetros físicos de las zonas de emisión de rayos gamma. Mientras que los largos pueden dar información sobre la precesión del jet o el flujo de acreción.

- De las 96 fuentes, se encontró que 41 son fuentes brillantes, que suelen estar asociadas con períodos prolongados de actividad elevada.
- En 20 de 96 fuentes, se observaron valores altos de flujo en la curva de luz ponderada en energía que sugieren diferentes escenarios físicos. Por un lado, se encontraron fotones de alta energía en algunos de los flares que aparecen tanto en la curva de luz pesada en fotones como en energía, lo que sugiere que la zona de emisión de rayos gamma podría estar fuera de la región de líneas anchas en el caso de los FSRQs. Por otro lado, se detectaron flares en la curva de luz de energía pero no en la de fotones, cosa que podría deberse a un endurecimiento espectral, donde el índice espectral disminuye, desplazando la emisión a energías más altas. Investigar este tipo de fuentes, en las que se detectaron fotones de altas energías, y en especial las más brillantes, es de gran interés para ser observados con telescopios Cherenkov.
- En distintas proporciones, se encontraron: fuentes donde un modelo de índice espectral dependiente del flujo fue favorecido sobre un modelo de índice constante para al menos uno de sus flares (36.45 % de las fuentes); en otras donde es favorecido sobre un flare global que engloba a todos sus flares y que por tanto hace que la fuente no se pueda comportar como si tuviera un solo flare (12.27 % de las fuentes con varios flares); en otras donde se cumplen las dos condiciones anteriores (sólo para 7 fuentes, un 12.73 % de las fuentes con varios flares y son todas FSRQ además); y en otras que para el flare global un modelo de índice espectral dependiente del flujo es significativo sobre un modelo de índice constante (14.55 % de las fuentes con varios flares). Estos resultados muestran que un modelo de índice espectral dependiente del flujo no es muy útil para explicar los datos, no sólo porque representa a un porcentaje muy bajo de las fuentes, sino también porque en la mayoría de los flares el índice fotónico permanece relativamente constante. También se llega a la conclusión de que el modelo de flare global no explica la realidad de los datos, es decir, no se pueden analizar las fuentes de múltiples flares como si sólo tuviesen uno.
- La dispersión de la diferencia entre el índice fotónico de los flares y la media del índice de la fuente ($\Delta\Gamma$) es estrecha y está centrada en cero. Estos resultados indican que el índice fotónico no varía significativamente durante los flares para la mayoría de las fuentes, que es lo esperado según la bibliografía.
- El efecto 'más duro cuando más brillante' se observó en 33 de las 41 fuentes brillantes (80 %), que es lo esperado según la bibliografía.

También se analizaron fuentes específicas: 3C 454.3 mostró una amplia gama de duraciones de flares y variabilidad rápida; PKS 1424-41 mostró un flare muy largo; NGC 1275 mostró duraciones de flares variables y una tendencia a ser 'más duro cuando más brillan te' contradiciendo estudios anteriores; y PMN J0948+0022 y 1H 0323+342 exhibieron propiedades similares a blazares a pesar de ser menos brillantes.

Las contribuciones del proyecto para el campo de las altas energías son: un nuevo método para definir los flares, análisis de una gran muestra de fuentes e interpretación con datos actualizados. Además, algunas sugerencias para futuras investigaciones son: i) utilización del catálogo más actualizado 4FGL-DR4; ii) exploración de otros modelos espectrales aparte de la ley de potencias; iii) investigación en más rangos de longitud de onda para obtener una visión holística de los procesos físicos involucrados en las emisiones de AGNs; iv) un uso de intervalos de datos temporales más cortos a 3 días.

Contents

List of Figures

List of Tables

1 Introduction

The most energetic radiation in the entire electromagnetic spectrum corresponds to gamma rays (energy greater than 100 KeV). These photons are produced by the most violent and extreme phenomena in the Universe. However, the Earth's atmosphere acts as an opaque barrier to much of the electromagnetic spectrum, absorbing most wavelengths shorter than ultraviolet (UV), many wavelengths between infrared and microwaves, and most of the longest radio waves. Therefore, despite their high penetrative power, gamma rays can only be directly detected from space, outside the Earth's atmosphere. At higher energies, the flux of gamma rays from celestial sources reaching the Earth decreases drastically with energy, following a power-law (PL) spectrum, as shown in Equation (1) (Bose, V. R. Chitnis, Majumdar, and Acharya 2022),

$$\frac{\mathrm{d}N}{\mathrm{d}E} \propto E^{-\Gamma} \tag{1}$$

where $\Gamma \sim 2 - 3$ is the spectral index.

If the gamma rays are energetic enough, they interact with the nuclei in the atmosphere and generate a cascade of secondary particles, called Extensive Air Shower. This shower contains charged particles that cause the atmosphere to emit Cherenkov radiation, which can be detected with ground-based telescopes, known as Imaging Atmospheric Cherenkov Telescopes (IACTs). At energies below 100 GeV, gamma rays generate cascades in the atmosphere, but the resulting images are small and difficult to distinguish from those caused by cosmic rays. Gamma radiation with photon energies of 100 GeV to 100 TeV is denoted as Very High Energy (VHE). Although 100 GeV is generally considered the limit for ground-based detection, Cherenkov telescopes, such as the upcoming CTA[1], will be able to detect energies as low as 30 GeV. Detecting such high energies requires large-area detectors and longer exposure times (Hillas 1985).

1.1 Gamma-ray generation in astrophysics

The Universe contains both thermal and non-thermal emissions, depending on the physical processes involved. For example, optical emissions from stars are characterised by black body radiation. In contrast, very high energy emissions originate from astrophysical sources powered by the release of gravitational energy and the relativistic acceleration of particles. The emission mechanisms in this spectral range involve subatomic particles, leptons or hadrons, accelerated to high velocities (Bose, V. R. Chitnis, Majumdar, and Shukla 2022). The main γ-ray emission processes are summarised as follows:

- **Inverse Compton (IC) Scattering:** a low-energy photon collides with an ultra-relativistic electron which transfer energy to the photon emitting a γ-ray photon.
- **Synchrotron Radiation:** radiation is emitted by highly energetic charged particles rotating in presence of an intense magnetic field. For relativistic particles, emission is transmitted in the direction of motion.
- **Curvature Radiation:** radiation is emitted by high-energy electrons accelerated by a curved magnetic field.
- **Bremsstrahlung:** radiation is emitted when a charged particle experiences a strong nuclear force while passing near an atomic nucleus, causing it to decelerate.
- **Decay of Neutral Pions:** when a proton collides with another proton or a photon, neutral (π^0) or charged pions (π^+/π^-) can be produced equally. Charged pions decay, producing a muon and a

[1] http://observatorio-cta.es/

neutrino, while neutral pions quickly decay emitting two γ-ray photons. Another physical process that produces neutral pions is the annihilation of particle-antiparticle pairs, such as an electron and a positron.

Gamma rays are detected from a diversity of celestial objects, including both galactic and extragalactic sources. Examples within our Milky Way are pulsars, X-ray binaries, or supernova remnants; and beyond our galaxy, relativistic jets of active galactic nuclei (AGNs), galaxies with star-forming bursts, or γ-ray bursts (Bose, V. R. Chitnis, Majumdar, and Shukla 2022).

The main processes of absorption or attenuation in this spectral range are the following:

- **Compton Scattering:** a high-energy photon loses energy when colliding with a free electron.
- **Pair Production:** when two photons with a combined energy equal to or greater than the rest mass energy of an electron and a positron ($E = 1.022\,MeV$) collide, there is enough energy to create an electron-positron pair.

These interactions between gamma rays (especially VHE photons) and low-energy electrons or photons primarily occur in gas and dust clouds found in active galactic nuclei, the intergalactic medium, and Earth's atmosphere. Under adequate conditions, the original γ-ray spectrum can be considerably modified by the electromagnetic cascades effectively developed through the absorption that creates energetic pairs and the subsequent inverse Compton emission from these pairs. Therefore, these processes are crucial for detecting gamma rays both in space and on Earth because what is detectable is the electromagnetic cascade produced (Bednarek 1997).

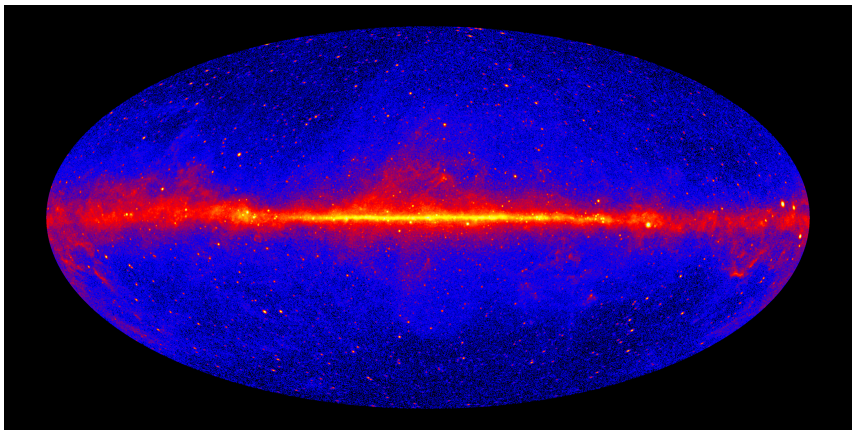

Figure 1: *Fermi's 12-year View of the γ-ray sky seen by Fermi-LAT with energies greater than 1 GeV. Image credit:* https://svs.gsfc.nasa.gov/14090/#section_credits.

The number of γ-ray sources known is very limited compared with lower wavelengths. In concrete, the last version of the fourth *Fermi*-LAT (see Section 2.1) catalogue (4FGL-DR4, for Data Release 4) contains 7194 γ-ray sources. This catalogue is based on the first 14 years of scientific data in the energy range from 50 MeV to 1 TeV (Ballet, Bruel, et al. 2023 & Abdollahi, Acero, Baldini, et al. 2022). Figure 1 shows the γ-ray sky map at $E > 1\,GeV$ based on *Fermi*-LAT 12-year observations. The central plane of our Milky Way galaxy is distinguished by a prominent, diffuse glow that extends along the middle of the map. Above and below the Milky Way plane, the emission is dominated by point-like sources, mainly AGNs.

1.2 Active Galactic Nuclei

Active Galactic Nuclei are the brightest central regions of a type of galaxy known as Active Galaxies, characterised by exceptionally luminous centres within a very concentrated volume fuelled by the process of accretion onto supermassive black holes (SMBHs). Some of these structures eject high speed material generating relativistic bipolar jets which can be extended over hundreds of kiloparsecs beyond their host galaxies[2]. AGNs serve as special laboratories for extreme physics and they are also key probes for studying the Universe on large scales, making their understanding essential for studying the formation and evolution of the Universe.

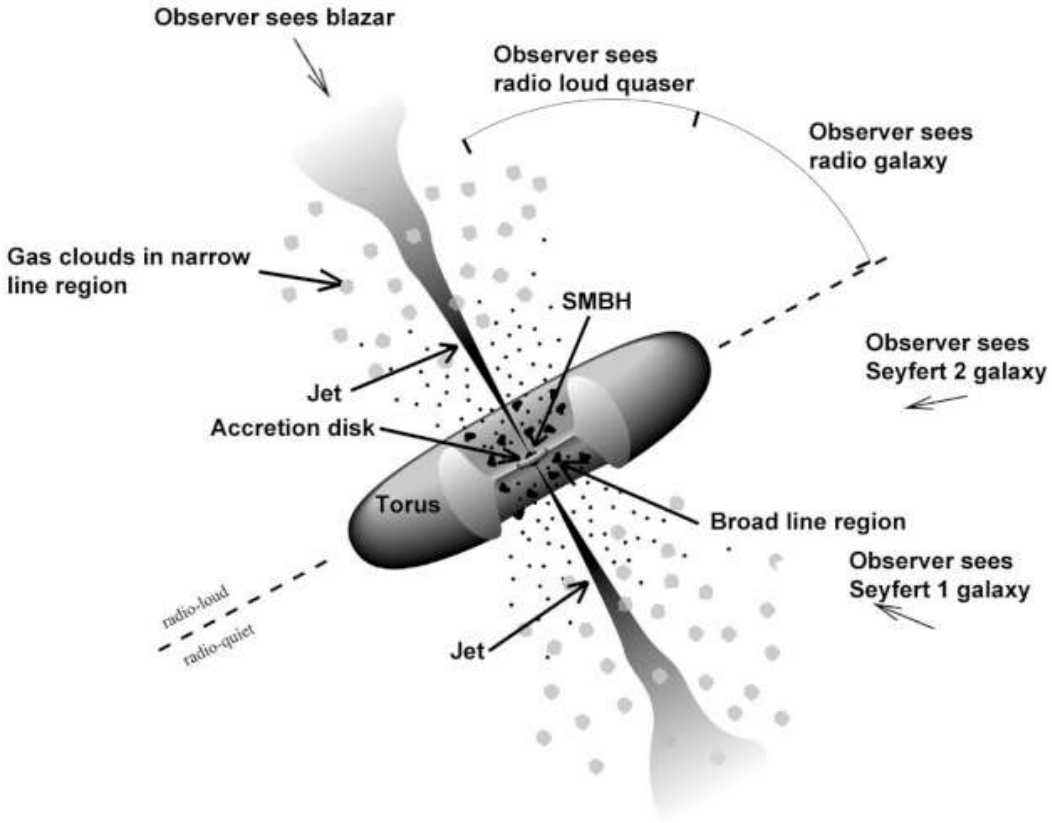

Figure 2: *General scheme of the unified model of AGN. Image credit:* https://fermi.gsfc.nasa.gov/science/eteu/agn/.

The full range of AGNs includes a variety of names, detection criteria, and characteristics related to spectra, polarisation, and temporal variability. Figure 2 shows a schematic representation of the Unification Model of AGNs, in which according to their orientation with respect to the line of sight, AGNs are classified as radio galaxies, quasars, blazars, or Seyfert galaxies (Urry and Paolo Padovani 1995). In Figure 2, the central SMBH is shown surrounded by the accretion disk, formed by matter falling into the black hole. The 'Broad Line Region' (BLR) shown in the diagram, characterised by rapidly moving gas clouds, may be located around the accretion disk. This region, also can be surrounded by a dusty torus. In the outermost regions of the AGN, there are gas clouds constituting the 'Narrow Line Region' (NLR). Finally, in some cases, the bipolar relativistic jet can be observed, originated from the vicinity of the central black hole (Bose, V. R. Chitnis, Majumdar, and Shukla 2022).

[2] https://fermi.gsfc.nasa.gov/science/eteu/agn/.

Each component of the AGN emits at different wavelengths. The accretion disk, the BLR, and the NLR emit in the optical/ultraviolet wavelengths; the dust torus in the infrared; the corona, which forms above the accretion disk, in X-rays (but this is not always observed); and the relativistic jet emits across the entire electromagnetic spectrum, being the only component that emits in gamma rays (P. Padovani et al. 2017).

It is possible to study these AGNs using their light curves (LCs), which represent the received photon flux over time. In these curves, 'flares' or 'outbursts' can be identified. These are defined as periods during which the source significantly boosts its flux in a temporal interval. They may manifest simultaneously across various wavelengths, display delays between different bands, or occur exclusively within a specific spectral range (Wang et al. 2022). They seem to appear spontaneously and are therefore impossible to predict. The time scales goes from minutes to years.

1.2.1 Blazars

When the AGN jets align with Earth, the AGN is called blazar. These specific AGNs appear extremely luminous across the entire electromagnetic spectrum, from radio to gamma rays, due to the relativistic Doppler effect. In this context, the process is known as Doppler boosting (or Doppler beaming or relativistic beaming), and it modifies the apparent luminosity of emitting matter moving at speeds close to the speed of light. It commonly occurs in the two oppositely-directed relativistic jets of plasma that originate from the SMBH that is accreting matter. Consequently, if the jet material is moving towards the observer (viewed 'head-on'), it will appear brighter than if it were at rest. Conversely, if the material is moving away, it will appear fainter or even invisible. While the relativistic outflow may occur throughout a wide cone, the observer sees only the portion of the cone moving close to the line of sight (Kellermann and Owen 1988).

Blazars are currently categorized into BL Lacertae objects (BLLs) and Flat Spectrum Radio Quasars (FSRQs). This classification distinguishes FSRQs as having optical emission lines with an equivalent width larger than 5 Å, while BLLs have an equivalent width under 5 Å or lack these lines entirely (Stickel et al. 1991). FSRQs also fit into the relativistic beaming model for radio sources, which unifies core-dominated and lobe-dominated sources based on orientation: core-dominated objects are viewed close to the jet axis, and lobe-dominated objects are viewed at larger angles (R. D. Blandford and M. J. Rees 1974). A radio-loud quasar, with powerful radio jets extending from subparsec to sometimes megaparsec scales, features a compact central core with a flat spectrum and two extended lobes with steep spectra. It appears as an FSRQ when core-dominated and as a steep-spectrum radio quasar (SSRQ) when lobe-dominated (Gaur et al. 2019).

The spectral energy distribution (SED) of both blazar subclasses is characterised by having two peaks, as shown in Figure 3.

The first peak is primarily attributed to synchrotron emission from relativistic electrons located in the jet emission zone. It allows further classification into low- (LSP), intermediate- (ISP), and high-frequency peaked sources (HSP). For the LSP, $\log \nu_{\text{peak}} < 14$; for the ISP, $14 < \log \nu_{\text{peak}} < 15$; and for HSP, $\log \nu_{\text{peak}} > 15$. For FSRQs, the first SED peak typically falls in the infrared (IR) regime (they are LSPs). However, for BLLs it spans from the IR to hard X-rays, therefore they can be LSPs (called LBL), ISPs (called IBL) or HSPs (called HBL). An observed anti-correlation seems to exist between the first peak's location and source luminosity: as the source luminosity increases, the first SED peak moves from higher to lower frequency across HBL, IBL, LBL, and finally to FSRQ. The reason for this effect is that the brighter the source, the more efficient the cooling of electrons, as they radiate energy through

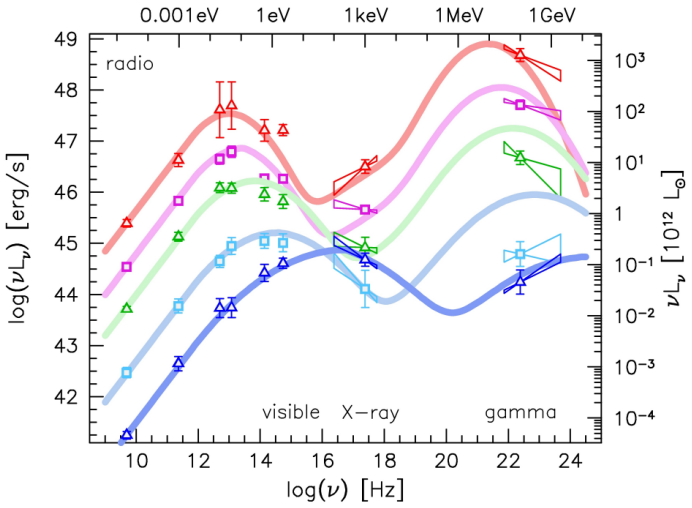

Figure 3: *SED for different types of blazars. From red to dark blue, the SEDs of FSRQ, LBL, IBL, HBL, and extreme HBL (TeV BLL blazar) are depicted. The lines represent the models, and the points represent the observational data for each blazar type. Image credit: R. Blandford, Meier, and Readhead 2019.*

synchrotron radiation and IC scattering (Hovatta and Lindfors 2019).

The second SED peak can originate from either hadronic or leptonic processes. On the one hand, in leptonic models, the emission is primarily driven by IC scattering. For BLLs, the accelerated electrons in the jet generate the observed emissions through IC scattering, in which the photons colliding with the ulta-relativistic electrons are those emitted as synchrotron radiation within the jet itself. This model is known as the 'synchrotron self-Compton' (SSC) model. In the case of FSRQs, where the second peak is significantly more intense than the first one, SSC emission alone is often insufficient to explain the observed radiation. Here, IC interactions occur between the same population of accelerated electrons producing synchrotron in the jet and either the photons produced by SSC or external photons from other parts of the AGN, such as the optical/UV photons emitted by the BLR and the infrared photons emitted by the dust torus. These scenarios fall under the category of 'external Compton' (EC) radiation models (Marek Sikora, Begelman, and Martin J. Rees 1994).

In leptonic models, the γ-ray spectrum's shape is directly influenced by the energy distribution of the accelerated electrons. This relationship is simple for IC scattering in the Thomson regime but becomes more complicated in the Klein–Nishina regime. The type of IC scattering regime is determined by the value of the target photon energy in the electron rest frame. In the Thomson regime, this value is smaller than $m_e c^2$, whereas in the Klein–Nishina regime, it is larger than $m_e c^2$ (Dermer and Menon 2009). When target photons originate from SSC or a dusty torus around the central accretion flow (resulting in EC on dust-torus emission), IC scattering to GeV γ-ray energies typically occurs in the Thomson regime. Conversely, when target photons originate externally from the BLR (resulting in EC on BLR emission), IC scattering to GeV energies typically occurs in the Klein–Nishina regime. According to the Klein–Nishina formula, which gives the differential cross-section of photons scattered from a single free electron, the total cross-section and the expected deflection angle decrease as photon energy increases. The electron distribution models are often represented by a broken power law, a log-parabola with a power law, or a power law with an exponential cutoff. Deviations of blazar γ-ray spectra from a pure power law may be due to an underlying electron population that deviates from a pure power law or/and the transition of the IC scattering process from the Thomson to the Klein–Nishina regime at higher γ-ray energies, where

scattering efficiency decreases as the effective cross-section diminishes (Van den Berg et al. 2019).

On the other hand, hadronic models propose that high-energy photons arise from the decay of neutral pions, generated through proton-photon interactions and annihilation of particle-antiparticle pairs in the vicinity of the jet (Mücke et al. 2003).

The precise location of the γ-ray emission zone within the jet remains uncertain (R. Blandford, Meier, and Readhead 2019). The timescale of flux variability provides insights into whether the emission region is closer or farther from the black hole. Assuming the emission region corresponds to the jet section and considering the conical shape of the jet, a larger jet section implies greater distance from the black hole. Consequently, faster variability suggests a closer proximity to the black hole than slower variability. Moreover, the duration of a brightening event provides information about the maximum size of the region where gamma rays are produced - the shorter the variability, the more compact the emission region. Therefore, the existence of outbursts with different variabilities in the same source may imply that the flaring state is caused by emission regions at different points in the jet or by different emission mechanisms.

Generally, γ-ray emission in blazars is believed to be associated with shocks travelling down the jet or with the jet formation region near the SMBH (Shukla et al. 2018). In EC models, the emission region must be located near the BLR or the dust torus to incorporate an external photon source for the jet (M. C. Nalewajko K. and M. Sikora 2014).

In the past, VHE photon emission has only been detected in HBL objects. Nevertheless, VHE photons have been observed from FSRQ, imposing significant constraints on jet emission and attenuation models within the BLR of AGNs. If the VHE photon emission zone in the jet is within the BLR, BLR photons interacting with VHE photons via pair creation would prevent the observation of VHE photons (Böttcher 2008). In BLLs, as there is no BLR, high-energy photons can es cape without interactions from the AGN.

1.2.2 Radio Galaxies

It is important to study γ-ray emission from radio galaxies (RDG) and quasars, particularly in the early stages of their evolution, because it provides information about the origin and structure of the radio jets.

Although blazars dominate the extragalactic γ-ray sky, a small percentage of γ-ray AGNs are radio galaxies (misaligned AGNs), which have larger jet inclination angles ($> 10°$). They offer a unique opportunity to explore non-thermal processes in AGN regions not affected by relativistic beaming, which are usually submerged into the beamed emission from the jet in blazars.

Quasars exhibit γ-ray emission due to smaller jet-inclination angles and beaming effects, while the origin of γ-ray emission in galaxies is still under debate. It is believed that the most powerful radio galaxies generate isotropic γ-ray emission through IC scattering of UV/optical/IR photons by electrons in the compact radio lobes (Principe et al. 2021).

1.2.3 Seyfert Galaxies

Seyfert galaxies, considered low-luminosity AGNs, are classified into Seyfert 1 and Seyfert 2 based on the presence or absence of broad permitted emission lines in their optical spectrum, respectively.

The narrow-line Seyfert 1 (NLSy1) galaxies are the Seyfert 1 galaxies which display broad permitted lines with small widths. The defining criteria include a full width at half-maximum (FWHM) of $H_\beta < 2000\,\mathrm{km\,s^{-1}}$, a weak [O III] emission line, and the presence of strong Fe II multiplets (Osterbrock and Pogge 1985 & Goodrich 1989). NLSy1s are generally radio-quiet, with only a small fraction being radio-loud (D'Ammando et al. 2013).

Detection of significant γ-ray emission from a few radio-loud NLSy1 galaxies (called γ-NLSy1) by *Fermi*-LAT (see Section 2.1) confirmed the presence of closely aligned relativistic jets in them. The origin of the radio-loudness in AGNs is often linked to central black hole properties (mass and spin) and accretion rate, but the physical processes ejecting the jet from the AGN core is still unexplained (Paliya et al. 2019). Therefore, *Fermi*-LAT observations revealed that although the extragalactic γ-ray sky is dominated mainly by blazars and some RDG, γ-NLSy1s are a possible third class of AGNs with relativistic jets. Notably, no radio-quiet Seyfert galaxies have been detected in gamma rays (D'Ammando et al. 2013). NLSy1s are commonly found in spiral galaxies with low-mass black holes at their cores (10^6 - $10^8\,\mathrm{M_\odot}$), postulated to be powered by high-accretion processes. Many NLSy1 galaxies exhibit features like a prominent soft X-ray excess, reflection-dominated hard X-ray emission, and brightness in X-rays.
γ-NLSy1 galaxies display rapid γ-ray variability, a curved γ-ray spectrum, and a Compton-dominated SED, features typically observed in FSRQs (Paliya et al. 2019).

1.3 Objectives and motivation of the work

The objectives of this work were considerably wide. They are listed below:

- To conduct a temporal analysis of the sources and their flares, looking at their light curves weighted by photons and energy. This was done for a sample of AGNs emitting extragalactic gamma rays between 0.1 and 100 GeV. The analysis utilised data available from the *Fermi*-LAT Light Curve Repository (Abdollahi, Ajello, et al. 2023) along with γ-ray properties from the same sources provided in the 4FGL-DR2 catalogue (Ballet, Burnett, et al. 2020 & Abdollahi, Acero, Ackermann, et al. 2020).

- To study the relationship between AGN types in terms of their power-law spectral index in the energy band from 0.1 to 100 GeV and how it behaves during their flares. This part was highly motivated by the lack of studies with such a large sample in the literature.

- The previous aims were set out as a systematic study of the whole sample of sources. Additionally, for specific sources with very strong features, an individual study of their γ-ray emission over time was conducted.

- To use the results obtained with *Fermi-LAT* to investigate which sources are interesting to observe with Imaging Atmospheric Cherenkov Telescopes.

2 Observations and data sample

As mentioned in Section 1, depending on the energy of the photon to be detected, the observation has to be done from space or from Earth. This work focuses on the analysis of data obtained by the Large Area Telescope aboard the *Fermi* space telescope.

2.1 *Fermi*-LAT

The *Fermi Gamma-ray Space Telescope*[3] (*Fermi*) of NASA is a space observatory that detects gamma rays in order to study the most energetic sky objects. Since it was launched on June 11, 2008 it has been monitoring the sky continuously. *Fermi* is the result of an international collaboration with contributions from space agencies, particle physics institutes, and universities in France, Germany, Italy, Japan, Sweden, and the United States. The spacecraft has two instruments aboard: 'Large Area Telescope' (LAT) and 'Gamma-ray Burst Monitor' (GBM).

The Large Area Telescope is the primary instrument on the *Fermi* mission. It is an imaging high-energy γ-ray telescope, sensitive to photons with energies from below 20 MeV to over 300 GeV. It has a wide field-of-view (FoV) of 2.4 sr with single photon angular resolution of 3.5° for 100 MeV and $\leq$ 0.°15 for E > 10 GeV, as shown in Figure 4 (left panel). LAT operates by monitoring the sky every 3-4 hours. Having a field of view covering approximately 20 % of the sky makes it an excellent instrument for detecting and observing sources whose intensity varies on short time scales, as it is the case of blazars. The Gamma-ray Burst Monitor complements the LAT's observations of transient sources by detecting X-rays and gamma rays within the 8 keV to 40 MeV energy range. Together, the GBM and LAT form a powerful system for investigating gamma-ray bursts, especially valuable for conducting time-resolved spectral studies across a broad energy spectrum.

Regarding the source sensitivity of the LAT, it depends on the flux and spectrum of the source. Figure 4 (right panel) represents the integral source sensitivity as a function of energy for different diffuse γ-ray background noise levels. It can be observed that beyond E > 10 GeV, the sensitivity is not very high given the low number of detected photons, making it challenging to obtain light curves from these energies. Nevertheless, although its capability to detect photons larger than 2 TeV is very small, combined with its full-sky coverage, it makes it a crucial instrument for triggering observations with Cherenkov telescopes (Atwood et al. 2009).

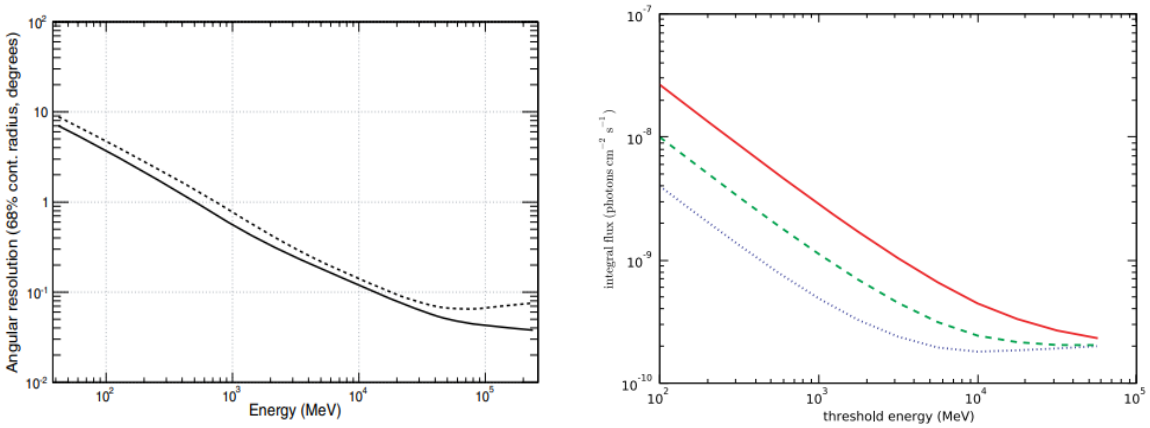

Figure 4: *In the left panel, angular resolution of Fermi-LAT, shown as the radius containing 68 % of the detected flux, where the solid curve represents normal incidence and the dashed curve incidence at 60°. In the right panel, sensitivity of Fermi-LAT for a 5σ detection for one-year of mission exposure. The source is assumed to have a power-law spectral index $\Gamma \sim 2$ and an integrated background flux (for E > 100 MeV) of 1.5×10^{-5}, 1.5×10^{-4}, and 1.5×10^{-3} ph cm^{-2} s^{-1} sr^{-1} for the blue dotted, green dashed, and red solid curves, respectively. Image credit: Atwood et al. 2009.*

[3] https://science.nasa.gov/mission/fermi/.

2.2 Data sample

The data sample analysed in this work was obtained from the 'Fourth *Fermi Gamma-ray* LAT catalog for Data Release 2' (4FGL-DR2)[4]. It is based on the first ten years of γ-ray data (from August 4, 2008, to August 2, 2018) in the spectral range from 50 MeV to 1 TeV, and it is an incremental update over the fourth source catalogue (4FGL) for the first eight years of LAT science data using the same analysis techniques. The catalogue has 5787 sources, including the original 4FGL sources. Figure 5 shows the 4FGL-DR2 catalogue sky map, where it is represented the 4FGL-DR2 sources distribution in the sky.

The light curves of 1500 sources from the 4FGL-DR2 sample are available in the 'Fermi LAT Light Curve Repository' (LCR)[5], where it is allowed to download data up to the most recent observations at the time of downloading. Since the data was downloaded in late 2022, the data used in this work spans 14 years.

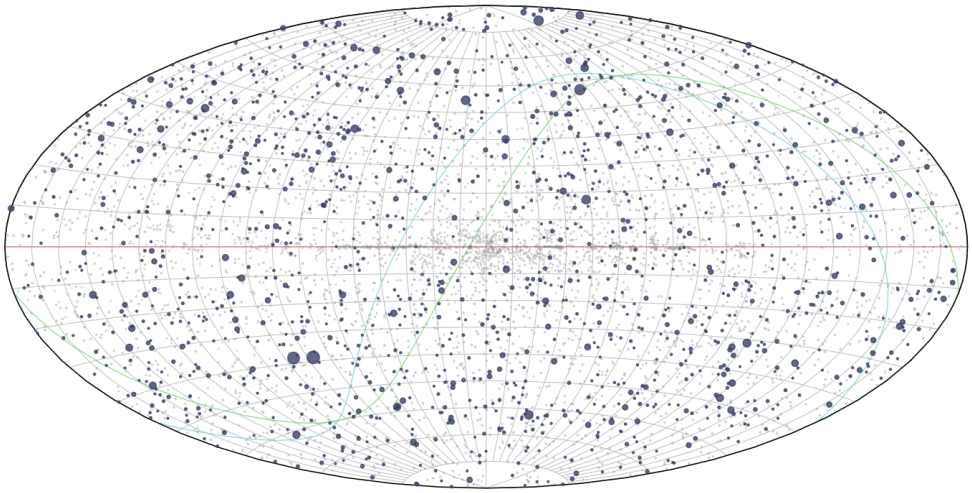

Figure 5: *4FGL-DR2 catalogue sky map. The coordinate planes are represented with colour curves being the red line the galactic plane, the green curve the ecliptic plane, and the blue curve the equatorial plane. The blue and grey markers are the sources with VI > 21.67 and VI < 21.67, respectively. For both, the size grows with the value of variability index. Image credit:* https://fermi.gsfc.nasa.gov/ssc/data/access/lat/LightCurveRepository/index.html.

The light curves of the LCR were produced for:

- Energy bins from 100 MeV to 100 GeV.
- Time bins of 3 day, 1 week, and 1 month.
- Sources with variability index greater than 21.67. The variability index (VI) serves as an indicator of the average fractional variability with the flux change relative to the average flux (dF/F) measured over yearly timescales. According to the 4FGL-DR2 catalogue, sources with a variability index exceeding 21.67 across 12 intervals are estimated to have less than a 1% probability of being constant sources.
- Photons within a 12° radius energy-independent region of interest centred on the source's location. The selection of the region of interest size is based on the 95 % containment radius of the LAT energy-dependent point-spread function (PSF) at 100 MeV.

[4] The downloaded filename, available as a FITS file to be used for data analysis within the Fermitools (https://fermi.gsfc.nasa.gov/ssc/data/analysis/documentation/), `gll_psc_v27.fit`, was obtained from: https://fermi.gsfc.nasa.gov/ssc/data/access/lat/10yr_catalog/.

[5] https://fermi.gsfc.nasa.gov/ssc/data/access/lat/LightCurveRepository/about.html.

- Minimum bin detection threshold of a test statistic (TS) of 1 - 4 (1 - 2 σ). The analysis for each bin detection employs a likelihood ratio test (Neyman and Pearson 1928), utilising a test statistic distributed as χ^2, to assess the significance of a source above the expected background. The TS is twice the ratio of the likelihood evaluated at the best-fit parameters under a background-only, null hypothesis. The null hypothesis is rejected when TS ≥ 4, equivalent to a 2 σ rejection criterion. For sources with TS ≥ 4, the analysis estimates the LAT flux and calculates upper limits for TS < 4 intervals using a Bayesian profile likelihood method.

3 Methodology

To complete this work, the Python programming language was employed. On one hand, a code from Josefa Becerra (one of the supervisors of this work) was used for LCR data downloading, applying the specific cutoff criteria mentioned below. On the other hand, a pipeline to process the light curves was developed from scratch. It permitted to obtain results, involving the analysis of sources to eliminate outlier points with obvious analysis errors (e.g. very extreme/unphysical flux values or spectral indices); the detection of sources with flares and the definition of flares; and ultimately, the calculations for generating the plots that illustrate the work outcomes based on the previously filtered data.

3.1 Data selection

The data time period studied in this work comprehend 14-year of *Fermi*-LAT data, from August 4, 2008, to November 22, 2022. The energy range is between 0.1 and 100 GeV. Therefore, integrating the expression (1) between these energies, the result is a flux in units of photons per area and time (photon flux units), as shown in Equation (2),

$$\int_{E_{\rm min}}^{E_{\rm max}} \frac{{\rm d}N}{{\rm d}E}{\rm d}E = \int_{0.1\,GeV}^{100\,GeV} N_0\,[{\rm ph\,cm^{-2}\,s^{-1}\,GeV^{-1}}] \left(\frac{\rm E}{\rm E_0}\right)^{-\Gamma} {\rm dE} = {\rm N\,[ph\,cm^{-2}\,s^{-1}]} \tag{2}$$

where N represents the photon flux; N_0 the photon flux per energy (photon flux density); and E_0 is the pivot energy. Pivot Energy is a reference energy chosen to coincide with the energy level where the relative uncertainty on the differential flux reaches its lowest point (i.e., the flux errors are minimal). It serves as an estimation of the point where the covariance of the power-law spectral index is minimised (Hassan et al. 2013). If the integrand is multiplied by the energy E, i.e. the photon flux is weighted by energy, the result is in energy per area per time (energy flux units).

As explained in Section 2.2, the downloaded catalogue has all the possible variability index values of 4FGL containing 5787 sources. Therefore, the initial applied criterion was to maintain only the sources with VI > 21.67 and to discard unknown objects retaining only BLLs, FSRQs, γ-NLSy1s, RDGs, and AGNs, which are sources with unclear classification. After this cutout, the final sample had a size of 1082 sources: RDG = 7, ANG = 19, γ-NLSy1 = 6, BLL = 478, FSRQ = 572. This catalogue was used as an input to download the light curve data of its sources. The conditions to load them were the following:

- A temporal cadence corresponding to bins of 3 days.
- A free photon index type. The photon index is the power-law spectral index (Γ) described in Equation (1) and (2) in the energy range between 0.1 and 100 GeV for 3-day bins. A shift from energy space (E) to frequency space (ν) shows that the photon flux as a function of frequency (F_ν) is proportional to $\nu^{-\Gamma+1}$, thus, $\nu\,F_\nu \propto \nu^{-\Gamma+2}$. Applying logarithms and representing $\log(\nu\,F_\nu)$ as a function of $\log(\nu)$ gives the SED. Therefore, the photon index parameter indicates the slope of the source at the second peak of the SED.

- A minimum TS of 4.
- An energy and a photon flux types. For both flux types, the conditions were: TS, flux, flux error, photon index, and photon index error must be positive; and flux error/flux < 1. However, for photon flux there was an additional condition to remove outliers, flux $< 10^{-4}\,\mathrm{ph\,cm^{-2}\,s^{-1}}$. For energy flux, there is no an imposed maximum threshold flux value because each photon is crucial at the highest energies.

The LCR light curves are derived from a systematic analysis of *Fermi*-LAT data. As a result, they occasionally include bins where the automatic data fitting pipeline failed to converge properly, leading to inaccurate fluxes and spectral indices. To filter out these erroneous bins, and rejecting outliers and high errors, a selection based on a set of generic rules was applied to retain only the values deemed physically sound. This was followed by a manual inspection to remove any remaining bins that passed the initial selection criteria.

For the case of the photon flux type, the applied criteria to filter the data were the following:

- Concerning the spectral index, it was set $\Gamma < 6$ because greater values are probably unphysical. For its error, it was fixed Γ error < 3 for low fluxes, the ones which value is below the 80 flux percentile. For higher fluxes, it is important to not discard the values because they could be essential at the time of defining a flare (see Section 3.2).
- Regarding the flux, it was set flux $<$ Median flux $+ 3\,\sigma$, where σ is the flux standard deviation. For high fluxes (flux values $\geq$ 80th percentile), the criterion for the flux error was set to flux error/flux < 0.4. For low fluxes, the criterion was adjusted to flux error $< 0.4 \cdot$ flux + median flux error to avoid removing values in the lower part of the light curves, which are important for establishing a background level. If outliers could not be removed with the initial criterion, the threshold was adjusted to 0.3 instead of 0.4. Any remaining outliers were manually removed.

For the case of the energy flux type, in general, there are few points in the light curve to can determine the outbursts and all of them are important. The aim in downloading the light curves in energy flux units was to obtain information about if a source is increasing the energy (not only the photon flux) during a flare. For this reason, the cutoffs applied were only for the flux (not Γ) and for the flux error only the 0.4 criterion was used (not the 0.3).

3.2 Flare definition

As discussed in Section 1.2, AGNs are highly variable sources. They often exhibit flaring activity where the emitted flux significantly increases, frequently accompanied by spectral changes. These emission changes can have a complex temporal structure, with overlapping peaks, making it difficult to precisely define when one flare ends and another begins. Additionally, due to the stochastic nature of AGN variability, there is no uniform 'background' flux level, complicating the distinction between 'flare' and 'quiescence' states (Abdo, Ackermann, Agudo, et al. 2010). The quiescence state refers to the time when the source is out of flare state.

Various definitions have been proposed in the literature. K. Nalewajko 2013 suggested a simple definition where a flare is a continuous period associated with a flux peak, during which the flux exceeds half of the peak value, reaching this lower limit exactly twice, at the beginning and end of the flare. Other statistical definitions using blocks of data have been proposed by Resconi et al. 2009 and Yoshida et al. 2023. Resconi et al. 2009 used Maximum Likelihood Blocks, a model-independent method designed to

identify data blocks with a constant rate in variable periods, providing statistical significance for each block. Yoshida et al. 2023 recommended using Bayesian Blocks (BBs), a flexible implementation of the Bayesian Blocks algorithm described by Scargle et al. 2013.

This section outlines potential criteria for defining a flare. Specifically, two statistical definitions are proposed and compared: the first is inspired by a simple threshold criterion based on the average flux during periods of increased flux; the second one uses a Bayesian Block analysis.

First, a visual inspection of the light curves of the sources (in photon flux units) was conducted to discard sources with no significant flux increases and to make an initial approximation of the outbursts. An example can be seen in the left panel of Figure 6, where the flare is represented by red points, the quiescence state by black points, and the background or baseline flux level by a grey continuous line. Additionally, the 'wings' of the flare are shown in turquoise points, representing the regions just before and after the flux increase, where the points are rising or falling, respectively. A flare may include minor peaks, but these are not considered separate subflares because the flux does not decrease to the baseline level between them.

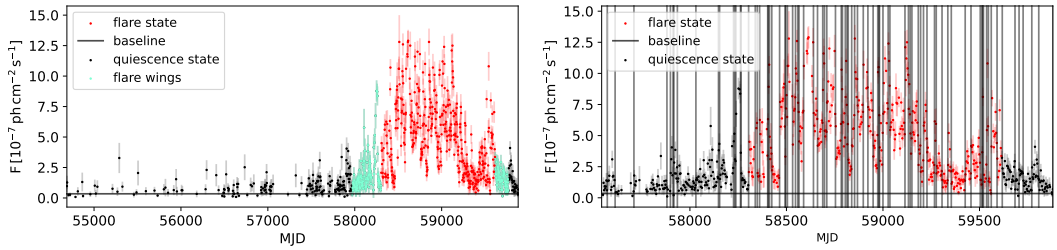

Figure 6: *Light Curve in photon flux units of the FSRQ 4FGL J0348.5-2749. The red points represent an example of how a flare was defined in the sample, and the black ones are the quiescence state points. The turquoise-coloured points are part of the quiescence state, but they show the 'wings' of the flare. Moreover, a grey continuous line is added to indicate the baseline. In addition, in the right panel, Bayesian Blocks are added as vertical grey lines and a zoom of the flare zone is done.*

Once an approximate flare selection was made, the first criterion was implemented to define when the source is in a flaring state by applying the concept of detection significance to the source's flux. Thus, it is considered that the source is in a flare at a specific time if the mean flux at that moment (f_{m1f}) minus the baseline value (and the mean flux of the points in quiescence state, f_{q}) is grater or equal to 5 times the mean flux error for the flare (σ_{1f}). This means, that Equation (3) is satisfied for $\mathrm{X} = \mathrm{bsl} + \varepsilon_{\mathrm{bsl}}$ and $\mathrm{X} = f_{\mathrm{q}} + \varepsilon_{f_{\mathrm{q}}}$, where bsl denotes the baseline (and $\varepsilon_{\mathrm{bsl}}$ its error) and $\varepsilon_{f_{\mathrm{q}}}$ is the error of f_{q}. Both $\varepsilon_{f_{\mathrm{q}}}$ and σ_{1f} were calculated as the standard deviation of the mean obtained in each case divided by the square root of the number of points.

$$f_{\mathrm{m1f}} - X \geq 5\,\sigma_{\mathrm{1f}} \tag{3}$$

The baseline was calculated as an approach of the flux in photon units taking into account all the source emissions as well as positive and negative fluctuations. The catalogue (4FGL-DR2) does not provide this value with this units, it provides the average integrated energy flux with energies from 0.1 to 100 GeV (energy_flux100) in units of erg cm^{-2} s^{-1} and the pivot energy (E_0 from Equation 2) in units of MeV, so the photon flux baseline was estimated as shown in Equation (4).

$$\mathrm{ph\_flux\_baseline}\,[\mathrm{ph\,cm^{-2}\,s^{-1}}] = \frac{\mathrm{energy\_flux100}\,[\mathrm{erg\,cm^{-2}\,s^{-1}}]}{\mathrm{E}_0\,[\mathrm{erg}]} \tag{4}$$

Note that from this equation, it is deduced that the error of the baseline has to be calculated as the energy_flux100 error (in erg cm^{-2} s^{-1}) divided by the pivot energy in units of erg. In energy flux units, the baseline is simply the energy_flux100 value.

After applying the first statistical criterion, the second one was used for comparison to see if the same points were included in the flare under both definitions. The Bayesian Blocks, implemented in the Python library `astropy.stats`, was employed for this purpose. This algorithm segments the light curve into parts, identifying significant changes in flux, indicating different behaviour of the source. By plotting a vertical line at each of these partitions and zooming in, it becomes easier to determine the start and end of a flare.

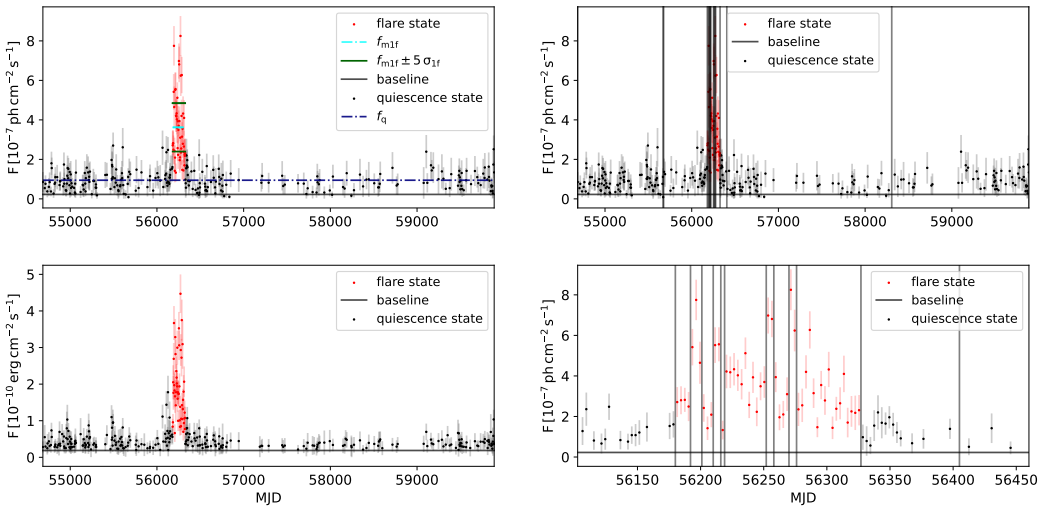

Figure 7: *Light curve of the FSRQ 4FGL J0830.8+2410 in photon flux units (upper panels and and bottom-right panel) and in energy flux units (bottom-left panel). Red and black points represent the flare and the quiescence state, respectively. In the upper-left panel, the mean flux value of the flare is shown in cyan, this mean* $\pm 5\,\sigma$ *in green, the baseline in grey and the mean of the points in quiescence in blue. In the upper-right panel, the Bayesian Blocks divisions are displayed as vertical grey lines, and the same in the bottom-right panel, but doing a zoom within the flare.*

In the left panels of Figure 7, the light curve of a source with a single strong flare (represented by red points) is shown. The upper-left plot displays the flare's mean flux value (and this mean $\pm 5\,\sigma$), the baseline, and the quiescence points (and their mean). The upper-right panel demonstrates that the Bayesian Blocks indicate a change in source behaviour only during the flare. The bottom-right panel provides a zoomed-in view, showing precisely where the change is completed. The complexity of the flare is reflected in the number of BBs identified; more blocks indicate more structures within a single flare. An example of a more complex flare is shown in the right panel of Figure 6. It was noticed that in some cases, the initial and final Modified Julian Date (MJD) values for the flares did not coincide between the two criteria. Therefore, the second criterion was used to delimit the flares when the two criteria differed.

Finally, a classification of sources with one flare and several flares (called single-flare and multi-flare sources, respectively) for all the AGN types was made. The final sources' set comprehend 96 sources, being 41 signle-flare sources (35 FSRQs, 5 BLLs, 1 γ-NLSy1) and 55 multi-flare sources (45 FSRQs, 8 BLLs, 1 RDG, 1 γ-NLSy1). Table 1 summarises these values, as well as the number of flares (for single-flare and multi-flare sources, including the total count) and the total number of sources for each AGN type.

	No. flares	No. sources	FSRQ	BLL	RDG	γ-NLSy1
Single-flare sources	41	41	35	5	0	1
Multi-flare sources	163	55	45	8	1	1
Total	204	96	80	13	1	2

Table 1: *Summary table of the number of sources for each AGN type from the sample in this work, classified according to whether they are single-flare or multi-flare sources. Also, it is included the number of flares for this last classification, as well as the total number of flares and sources.*

3.2.1 Flare Length and Brightness

Blazar flares can be categorised based on their duration into three types: year-long flares (last for a year or more, Chen et al. 2013); day-to-month-long flares (from a few days to several months, Impiombato et al. 2011); and intraday flares (occur within a single day, Wagner and Witzel 1995). Year-long flares may be associated with the orbital motion of a binary or jet precession (Ostorero, Villata, and Raiteri 2004), or instabilities in the accretion flow (Tchekhovskoy, Narayan, and McKinney 2011). In contrast, day-to-month-long and intraday flares are likely related to processes occurring within the jet itself. These shorter-duration flares can be explained by models involving one or more compact γ-ray emission zones in the jet (Rani et al. 2013). Therefore, observing day-to-month-long and intraday flares, including their temporal variability and spectra, can help constrain the physical parameters of the γ-ray emission zones, such as size, location, geometry, particle acceleration or cooling processes, among others.

In this work, since 3-day bins were used, it is not possible to define intraday flares, and it is very difficult to identify flares lasting less than a month (as a month is sampled by 10 bins). For this reason, a statistical method was employed to define the flare length based on the total length of the current light curve of the sources.

A histogram was created to represent the percentage of time each flare occupies in relation to the total duration of the light curve (upper panel of Figure 8), in this case a period of 14 years and 4 months (5163 days). Additionally, the median (Med) and standard deviation (σ) of the entire flare population were calculated. Flares with a duration below the median minus $\sigma/2$, which is 4.81 % of the LC or 8.2 months, were classified as short flares (27.94 % of all flares). Those with a duration above the median plus $\sigma/2$, 11.87 % of the LC equivalent to 1.7 years, were classified as long flares (27.45 % of the flares). Flares with duration between these two extremes were considered of medium length (44.61 % of the flares). In terms of the number of bins, short flares contain up to 83 bins, while long flares exceed 204 bins. This approach to defining flare length can be assumed for any light curve duration, as it relies on the idea that a minimum number of bins is needed to establish statistical significance to consider a flare, as shown in expression (3). Therefore, it is reasonable to consider a flare as short if it spans from the minimum number of bins to $\sim$ 83 bins. Similarly, flares longer than roughly 1 year and 8 months are deemed long flares. Consequently, it could be considered that medium and long length flares are into day-to-month-long and year-long flares classification, respectively.

For the brightness of the flares, another histogram was created, this time displaying the significance of the flare mean flux value relative to the quiescence state (bottom panel of Figure 8). Bright flares were defined as those with a significance above the median plus $\sigma/2$. That is $12.57\,\sigma_{1f}$, which correspond to 32.35 % of the flares.

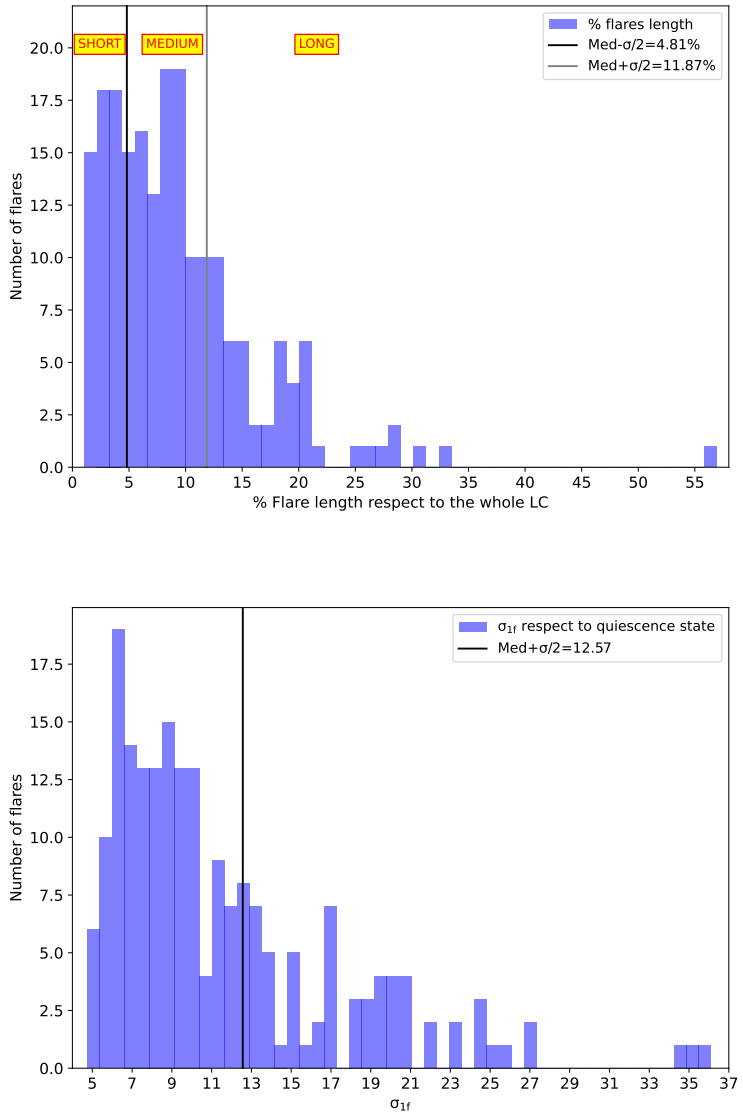

Figure 8: *Histograms used for defining the length and brightness of the flares, respectively. The upper panel represents the percentage of time for each flare relative to the total duration of the light curve. In it is shown the distribution of short, medium, and long flares based on the median and standard deviation values. The bottom panel displays the significance of the flare mean flux value relative to the quiescence state. The black vertical line delimits from which significance flares are considered bright based on the median and standard deviation values as well.*

3.3 Photon index analysis

As mentioned in Section 1.3, one of the work goals is to analyse the photon indices of the sources and how they change during the flares. The procedure to complete this task was accomplished in two parts:

1. To plot the photon index as a function of the photon flux to apply different linear fits. For each flare, the general fit was a linear equation in slope-intercept form $y = m\,x + n$, where 'm' is the slope, and 'n' the y-intercept, both free parameters. This fit means that the photon index linearly varies with the photon flux during a flare. Furthermore, a fit in the form $y = n$ (which means that the photon index remains constant during an outburst) and $y = m\,x + ct$ were applied. In the latest,

the y-intercept is a constant calculated as a weighted average of the n-values of the fit $y = m\,x + n$ where the weights are 1 over the n-value errors. This fit was considered to make the linear fit more robust because it may be unstable with all parameters free (the n-values may vary significantly from each other). Additionally, for the multi-flare sources, a global flare was defined as the sum of all the flares together using a mask, 'forcing' the source behaving as a single-flare source. For this global flare, also the fits $y = m\,x + n$ and $y = n$ were employed.

To obtain all the free parameters (m,n or n) and their covariance matrix, the `curve_fit`[6] algorithm of the python library `scipy.optimize` was used [7]. The errors of the free parameters were calculated from the square root of the diagonal elements of the covariance matrix associated with each value. A χ^2 significance test was used to compare the results from the fit $y = m\,x + n$ and from the fit $y = n$ for each individual flare and for the global flare. For each fit, χ^2 is calculated as follows:

$$\chi^2_{\text{fit}} = \sum \frac{(y_{\text{fit}} - y_{\text{data}})^2}{y^2_{\text{error}}} \tag{5}$$

Therefore, if $\chi^2 = \chi^2_{\text{fit0}} - \chi^2_{\text{fit1}} > 0$, fit 1 is preferred over the fit 0 (the higher χ^2_{fit} the worst statistics). To determine how greater the χ^2 value should be to has a reasonable significance, a $3\,\sigma$ significance criterion was considered using the python library `scipy.stats.chi2`[8]. Specifically, σ is calculated using both χ^2 and ndf, which is the difference in the number of degrees of freedom of the two fits. In the case of this work, $ndf = ndf_{\text{fit0}} - ndf_{\text{fit1}} = (\text{N - 1}) - (\text{N - 2}) = 1$, where N = number of points; $ndf_{\text{fit1}} = (\text{N - 2})$ because in the $y = m\,x + n$ fit two parameters are adjusted (two degrees of freedom, m and n); and $ndf_{\text{fit0}} = (\text{N - 1})$ because in the $y = n$ fit there is only one free parameter (n). Thus, if $\sigma > 3$, fit 1 has a higher significance over the other one, if not, both fits are considered statistically indistinguishable.

Another significance test used in this work was employed to determine if a single flare is significant over the global flare fit. For this, a $3\,\sigma$ significance criterion was applied as well. In this case, σ was obtained in the following manner:

$$\sigma = \frac{m_{\text{1f(n=ct)}} - m_{\text{global}}}{max(\varepsilon_{m_{\text{1f(n=ct)}}}, \varepsilon_{m_{\text{global}}})} \tag{6}$$

where $m_{\text{1f(n=ct)}}$ is the m value of the fit $y = m\,x + ct$ and $\varepsilon_{\text{m}_{\text{1f(n=ct)}}}$ its uncertainty; and m_{global} is the m value of the fit $y = m\,x + n$ of the global flare and $\varepsilon_{m_{\text{global}}}$ its uncertainty.

2. To measure the hardness of the sources during flaring states. In the γ-ray community terminology, sources are often classified as 'hard' or 'soft' depending on their photon index Γ. During flare events, the spectra of some sources can change, becoming harder when Γ decreases or softer when Γ increases. In general, a source is harder when brighter (Abdo, Ackermann, Ajello, et al. 2010). In order to quantify whether becomes harder or softer, an average variation of photon index ($\Delta\Gamma$) during flares was calculated as shown in Equation (7),

$$\Delta\Gamma = (avg_{\Gamma_{\text{fls}}} + \varepsilon_{avg_{\Gamma_{\text{fls}}}}) - (avg_{\Gamma_{\text{S}}} + \varepsilon_{avg_{\Gamma_{\text{S}}}}) \tag{7}$$

where $avg_{\Gamma_{\text{fls}}}$ is obtained by using the global flare mask to average the Γ of all these points and $\varepsilon_{avg_{\Gamma_{\text{fls}}}}$ its error (calculated as the mean standard deviation divided by the square root of the number of points); and $avg_{\Gamma_{\text{S}}}$ is the source mean Γ and $\varepsilon_{avg_{\Gamma_{\text{S}}}}$ its error, both obtained from the catalogue (4FGL-DR2). By definition, if $\Delta\Gamma < 0$, the source is getting harder during the flares.

[6] https://docs.scipy.org/doc/scipy/reference/generated/scipy.optimize.curve_fit.html.
[7] Only the y-axis errors ware taken into account as weights, but the x-axis errors are related with the y-axis ones.
[8] https://docs.scipy.org/doc/scipy/reference/generated/scipy.stats.chi2.html.

4 Results and Discussion

The subsequent analysis of the sources and their flares, conducted to achieve the objectives outlined in Section 1.3, is structured into two parts. The first part, Section 4.1, provides a comprehensive overview of the temporal and photon index analysis of the sources within the sample. Based on these general findings, particular attention is given to select sources that exhibit notable characteristics or are deemed especially interesting for further discussion in Section 4.2. Furthermore, a physical interpretation of the results is made.

4.1 General results

4.1.1 Temporal analysis

Studying the length and variability of flares is particularly interesting, as mentioned in Sections 3.2.1 and 1.2.1, respectively. Variability indicates that non-thermal emission might originate at different distances from the black hole in the jet and that the emission regions can vary in compactness. On the other hand, different duration timescales may correspond to different aspects of blazar and jet physics.

In this study, defining rapid or slow variability is extremely challenging because the 3-day time intervals are relatively large to sample this property well. For this reason, the focus has been more on the length of the flares rather than on their variability.

The following quantities were found for each of the lengths defined in Section 3.2.1: 46 sources have at least a long flare, 31 have at least a short flare, and 12 have at least a short and a long flare. This last number represents the most varying sources of the sample, being 12.5 % of the total sources and 21.82 % of the multi-flare sources as all 12th sources are found in this category.

Regarding the bright sources, defined as those with at least a bright flare (defined in Section 3.2.1), 41 out of 96 sources were classified as bright. Therefore, almost half of the objects of the sample are bright (42.70 %), and most of them include long flares. Specifically, 29 sources are bright along with long flares, but only 13 sources are bright with short flares. In Table 2 is shown how the previous numbers are distributed among the different types of AGN. An additional row is added to the table, providing a summary of the total number of sources and their breakdown by AGN type, as shown in the last row of Table 1.

	FSRQ	**BLL**	**RDG**	**γ-NLSy1**	**Total**
Bright	34	6	1	0	41
Long flares	39	6	1	0	46
Short flares	23	5	1	2	31
Long + short flares	10	1	1	0	12
Bright + long flares	24	4	1	0	29
Bright + short flares	10	2	1	0	13
AGN type summary	80	13	1	2	96

Table 2: *Summary table of the number of sources of each type of AGN that meet the criteria of being bright, having long flares, having short flares, having long and short flares at the same time, and being bright with either long or short flares simultaneously. The last row provides a summary of the total number of sources and their classification by AGN type.*

Moreover, high flux values on the energy-weighted light curve were observed for 20 of the 96 sources, indicating two different physical scenarios.

On the one hand, high-energy photons were detected in some of the flares appearing in both the photon- and energy-weighted light curves (evidenced by the high intensity of the flare in the energy light curve). This suggests for the case of the FSRQs, that the γ-ray emission zone might be outside the BLR, allowing high-energy photons to escape without being absorbed. Despite the small number of high-energy photons, the total photon count is sufficient to detect an outburst in the photon flux light curve, indicating a highly efficient γ-ray emission mechanism. These flares are called 'strong flares in energy LC' in Table 3.

On the other hand, some flares were detected in the energy light curve but not in the photon one, which could be due to spectral hardening. This means that the photon index measured by *Fermi*-LAT decreases, likely indicating a shift toward higher energies in the high-energy component of the SED (the second peak, see Figure 3). In such cases, the presence of only a few high-energy photons means that flares cannot be detected in the photon light curve. For FSRQs, also the emission zone outside the BLR is another possible explanation. These flares are called 'new flares in energy LC' in Table 3.

Investigating such sources in which high-energy photons have been detected (especially the brightest ones), is of significant interest for Cherenkov telescopes, as they provide opportunities to gain deeper insights into the high-energy photons received.

For this number of sources (20/96), it was found that almost all of them are FSRQs (15/20). However, there is no clear representation of the flares length in the sources because short, long, and medium flares are found in similar proportions. Additionally, 8 of these 20 sources are bright (in photon flux units) being 6 sources that become harder when brighter. Table 3 provides an itemisation of all these numbers for each type of AGN. Also, a last row is added to the table summarising the total number of sources and their categorisation by AGN type.

	FSRQ	**BLL**	**RDG**	**γ-NLSy1**	**Total**
Strong flares in energy LC	6	4	0	1	11
Strong flares in energy LC + bright	1 H + 1 S	1 H	0	0	3
Strong and new flares in energy LC	9	0	0	0	9
Strong and new flares in energy LC + bright	4 H + 1 S	0	0	0	5
AGN type summary	80	13	1	2	96

Table 3: *Summary table of the number of sources for each AGN type that meet the criterion of having strong flares in the energy light curve (first row) and this criterion alongside having new flares in the energy light curve which do not exist in the photon light curve (third row). In the second and fourth rows, each of these criteria are fulfilled in addition to being bright, respectively, indicating how many sources become harder (H) or softer (S) during flares for each type of AGN. In the fifth row, a summary of the total number of sources and their division by AGN type is provided.*

An example of one of the nine sources which meet the criteria of having strong and new flares in energy light curve is shown in the Figure 9 and the other eight sources with the same features are displayed in Appendix B. For the case in Figure 9, on the one hand, the red flare is intense in the energy light curve, reaching almost a flux value of $18\times10^{-10}\,\mathrm{erg\,cm^{-2}\,s^{-1}}$. On the other hand, a new flare in the energy light curve is observed at MJD $\sim$ 56850.

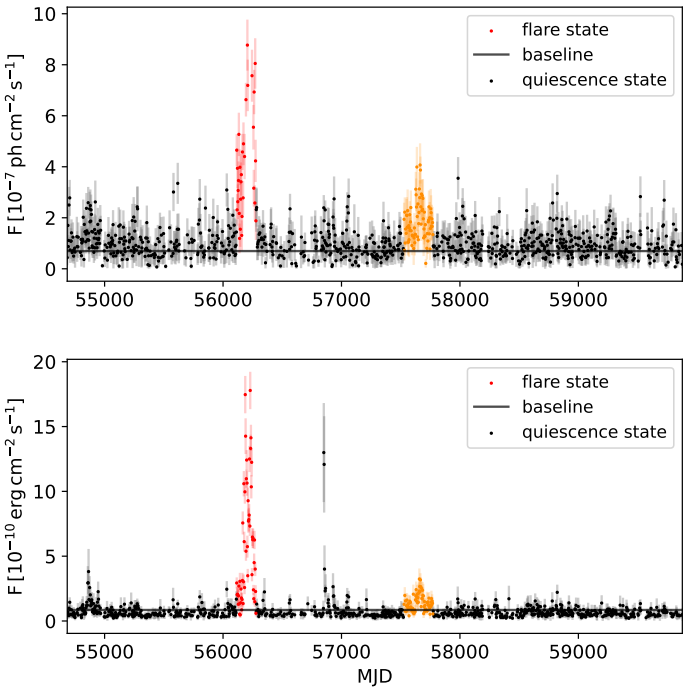

Figure 9: *Light Curve in photon flux units (upper panel) and in energy flux units (bottom panel) of the FSRQ 4FGL J0221.1+3556. This source meet the criteria of having strong and new flares in its energy light curve. The colour points represent the several flares of the source identified in this work, being the red one the strongest in the energy-weighted light curve. The black points represent the quiescence state, except for the ones describing the new flare observed at MJD ∼ 56850 in the energy-weighted light curve. The baseline is represented as a grey continuous line in both plots.*

4.1.2 Photon index analysis

Concerning the analysis of the photon index during flaring states, it was observed that a model with flux-dependent spectral index is favoured (at $3\,\sigma$, as explained in Equation 5) over a constant spectral index model ('Condition 1' in Table 4) for 18.75 % of the flares, which corresponds to 45 flares out of 204 found in 35 sources (36.45 % of the sources).

Among these 35 sources, 25 exhibit enhanced brightness during outbursts, with 21 becoming harder (H) and only 4 becoming softer (S). Regarding flare duration, 25 out of these 35 sources have long-duration flares in their light curves, while 12 have short-duration flares. Table 4 provides a breakdown of these numbers for each type of AGN. An additional row is added to the table, providing a summary of the total number of sources and their categorisation by AGN type, as shown in the last row of Table 1.

The fulfilment of the Condition 1 means that the photon index linearly varies with the photon flux during a flare. However, the slope value (m) provide the interpretation of whether the variation is positive or negative. By examining the histogram in Figure 10, it is evident that the most of the flares have a slope centred around 0, indicating that the photon index Γ remains relatively constant during a flare. This observation is supported by the Γ vs. MJD plot shown in the bottom-right panel of Figure 11 (presented below), where the dispersion in the y-axis is lower for the flares (colour points) compared to the quiescence state points (black points). Furthermore, Figure 10 illustrates that, generally, the slope is positive for BLLs and negative for FSRQs. This model is not very useful in explaining the data, not only because it is true for only almost 19 % of the flares, but also because, as shown in Figure 10, in most of the flares the photon index remains relatively constant.

	FSRQ	BLL	RDG	γ-NLSy1	Total
Condition 1	29	5	1	0	35
Condition 1 + bright	17 H + 4 S	3 H	1 H	0	25
Condition 1 + long flares	21	3	1	0	25
Condition 1 + short flares	9	2	1	0	12
AGN type summary	80	13	1	2	96

Table 4: *Summary table of the number of sources for each AGN type where a significant dependency of the spectral index with the flux is found ('Condition 1', first row). In the second, third, and fourth rows, this condition is achieved alongside other attributes which are being bright, having long flares, and having short flares, respectively. In addition, in the second row, it is indicated how many sources become harder (H) or softer (S) during flares for each type of AGN. In the fifth row, a summary of the total number of sources and their breakdown by AGN type is added.*

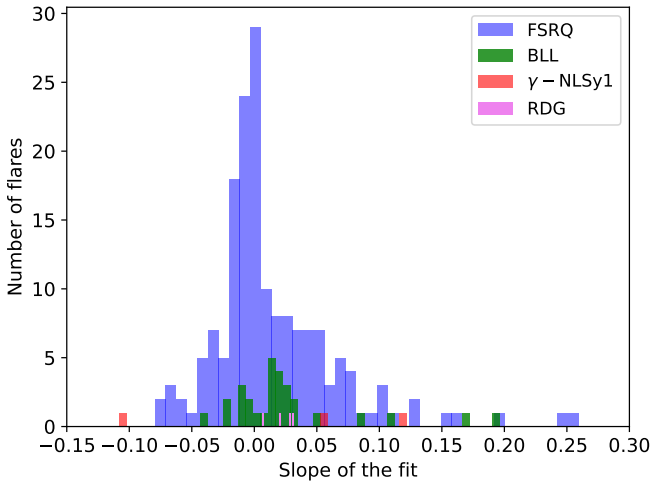

Figure 10: *Histogram illustrating the distribution of the slope (m) of the fit $\Gamma = m \cdot Flux + n$ in all the flares of the sample for each type of source.*

Continuing with the analysis of the fits for multi-flare sources, it was observed that 12.27 % of them show a statistically significant linear fit $\Gamma = m \cdot Flux + n$ (at $3\,\sigma$, as explained in Equation 6) over the global flare fit ('Condition 2' in Table 5). This corresponds to 20 out of 163 flares, representing 17 sources out of 55, with 14 being FSRQs and 3 BLLs. These sources cannot be analysed as single-flare sources because they have at least one flare statistically significant over the global flare. Among these 17 sources, 12 are bright with 8 becoming harder (H), and only 4 becoming softer (S) during flaring states. Moreover, 11 have long flares in their light curves, while 10 have short flares. Table 5 shows the classification by AGN type in the first four rows.

Additionally, only 7 out of 163 flares (4.29 %) from 7 sources (12.27 % of the multi-flare sources and all of them are FSRQs) satisfy the two previous conditions ('Condition 3' in Table 5): statistically significance of the fit $\Gamma = m \cdot Flux + n$ over both $\Gamma = n$ ('Condition 1'), and the global flare fit ('Condition 2') for flares of multi-flare sources. Thus, for these sources the same as Condition 1 and 2 is fulfilled together. This is that the photon index linearly varies with the photon flux for at least during one flare and this flare is significant over the global flare, so these sources cannot be analysed as if they were single-flare sources.

Of these 7 sources, 6 exhibit increased brightness during flares, with 4 becoming harder (H) and 2 softer (S). Regarding flare duration, 6 have long-duration flares in their light curves, while 5 have short-duration flares. These details are presented in the fifth to eighth rows of Table 5.

In terms of the global flare, a model with flux-dependent spectral index is favoured (at $3\,\sigma$, as explained in Equation 5) over a constant spectral index model ('Condition 4' in Table 5) in only 8 out of 55 sources, with 5 being FSRQs and 3 BLLs. This means that when forcing the source to behave as a single-flare source, the photon index linearly varies with the photon flux for 14.55 % of the multi-flare sources. This result is rather unfavourable, thus, it leads to the conclusion that it is not a model that explains the reality of the data, and the multi-flare sources cannot be analysed as if they had a single flare. Among these 8 sources, 7 are bright, with 5 becoming harder (H) and 2 becoming softer (S) during flaring states. Furthermore, 6 have long flares in their light curves, while only 3 have short flares. Table 5 provides a division of these numbers for both types of AGN between ninth and twelfth rows. An extra row is added to the Table 5, providing a summary of the total number of multi-flare sources and their distribution by AGN type, as shown in the middle row of Table 1.

	FSRQ	**BLL**	**RDG**	**γ-NLSy1**	**Total**
Condition 2	14	3	0	0	17
Condition 2 + bright	6 H + 3 S	2 H + 1 S	0	0	12
Condition 2 + long flares	8	3	0	0	11
Condition 2 + short flares	9	1	0	0	10
Condition 3	7	0	0	0	7
Condition 3 + bright	4 H + 2 S	0	0	0	6
Condition 3 + long flares	6	0	0	0	6
Condition 3 + short flares	5	0	0	0	5
Condition 4	5	3	0	0	8
Condition 4 + bright	3 H + 1 S	2 H + 1 S	0	0	7
Condition 4 + long flares	3	3	0	0	6
Condition 4 + short flares	2	1	0	0	3
multi-flare AGN type summary	45	8	1	1	55

Table 5: *Summary table of the number of multi-flare sources for each AGN type that meet the criterion of: having a model with flux-dependent spectral index favoured over the global flare fit for at least one flare ('Condition 2', between the first and fourth rows); having a model with flux-dependent spectral index favoured over both a constant spectral index and the global flare fit for at least one flare ('Condition 3', between the fifth and eighth rows); and for the global flare having a model with flux-dependent spectral index favoured over a constant spectral index ('Condition 4', between the ninth and twelfth rows). To each of these criteria, it is added other attributes: being bright, having long flares, and having short flares. In addition, for the case of brightness, it is indicated how many sources become harder (H) or softer (S) during flares for each type of AGN. The last row provides a summary of the total number of multi-flare sources and their breakdown by AGN type.*

An example of all the fits performed (except $\Gamma = \mathrm{m}\cdot\mathrm{Flux} + \mathrm{ct}$) can be seen in the first four panels of Figure 11. The data points (obtained from the catalogue 4FGL-DR2) are represented with a grey colour scale to show the density of points, with the maximum (white zone) located near $\Gamma \sim 2$ at low fluxes. The blue and grey error bars represent the points corresponding to the flare and quiescence state, respectively. For the individual fits (first row of the figure), each colour correspond to each flare of the same colour in the light curve in the bottom-left panel of Figure 11. The flares have different length: the red one is long, the orange one is short, and the magenta and green flares have intermediate duration. The middle row plots correspond to the global flare fits. It should be noted that although for cosmetic purposes (and for visual clarity) the errors in the parameters are omitted from the legends, they were calculated

as explained in Section 3.3 and properly saved for further calculations.

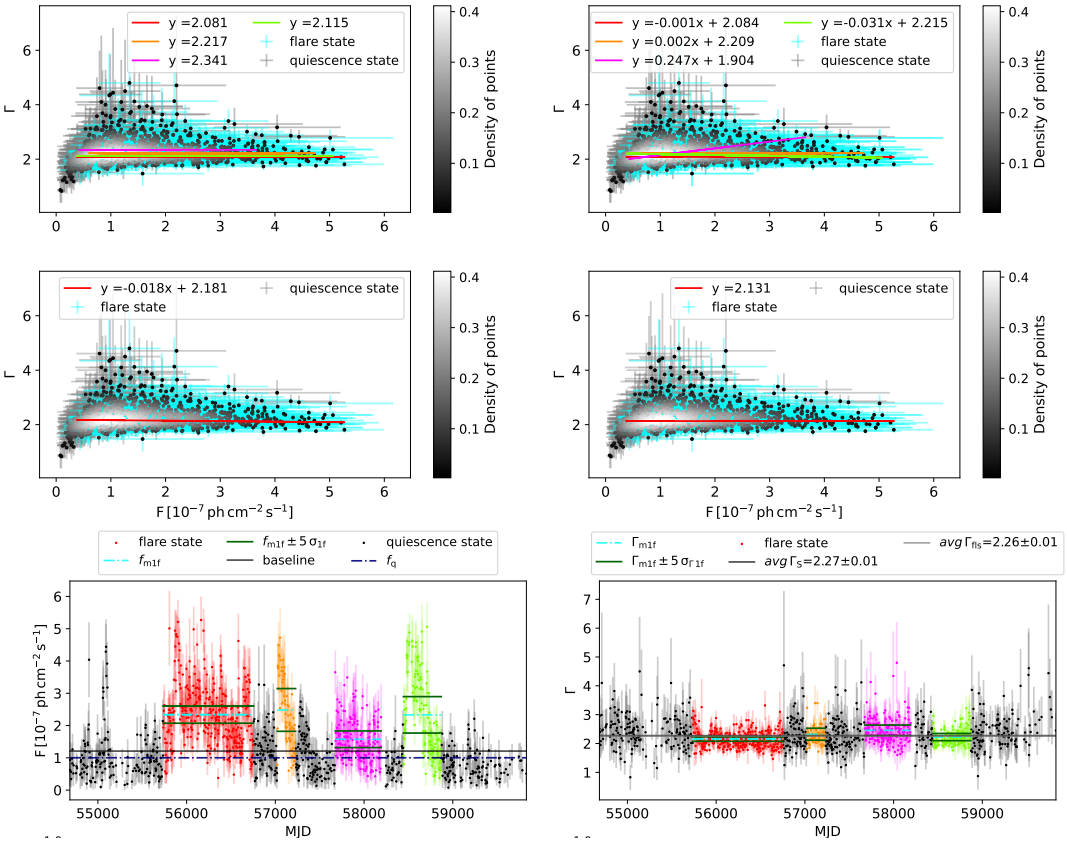

Figure 11: *Fits of photon index performed (except $\Gamma = m \cdot Flux + ct$) can be seen in the first four panels for the case of the FSRQ 4FGL J1345.5+4453. The data points are represented with a grey colour scale to show the density of points. The blue and grey error bars represent the points corresponding to the flare and quiescence state, respectively. For the individual fits (first row of the figure), each colour correspond to each flare of the same colour in the light curve in photon flux units (bottom-left panel) and the photon index vs. MJD plot (bottom-right panel). The middle row plots correspond to the global flare fits. In the bottom panels the flare mean (in cyan) and this mean $\pm 5\sigma$ (in green) are represented for the y variable, being the flux in the light curve plot and the photon index in the other. The black points represent the quiescence state. In addition, the baseline in grey and the mean of the points in quiescence in blue are shown in the light curve plot. For the case of the latest plot, the source mean Γ (avg_{Γ_S}) and the average photon index of the global flare mask ($avg_{\Gamma_{fls}}$) are shown as a black and grey line, respectively.*

Next, a brief overview of the distribution of Γ for the sources is provided. The left histogram of Figure 12 shows that the sources mean photon index is higher for FSRQs than for BLLs, meaning that FSRQs are softer than BLLs. This implies, therefore, that the second peak of the SED is at a lower energy in FSRQs than in BLLs. This is because as FSRQs are brighter than BLLs, they can be observed at greater distances (higher redshift), and thus, the peak is seen at lower energies. To properly evaluate this effect, a redshift correction would be necessary. This result is consistent with those presented by Abdo, Ackermann, Ajello, et al. 2010, and it is noticeable in Figure 3. Regarding the γ-NLSy1s and RDGs, although the sample may not be representative, it appears that the trend is that γ-NLSy1s are softer than RDGs. This trend would be consistent with the fact that the properties of γ-NLSy1s resemble those of FSRQs.

The histogram on the right of Figure 12 shows the distribution of the hardness of the sources during the

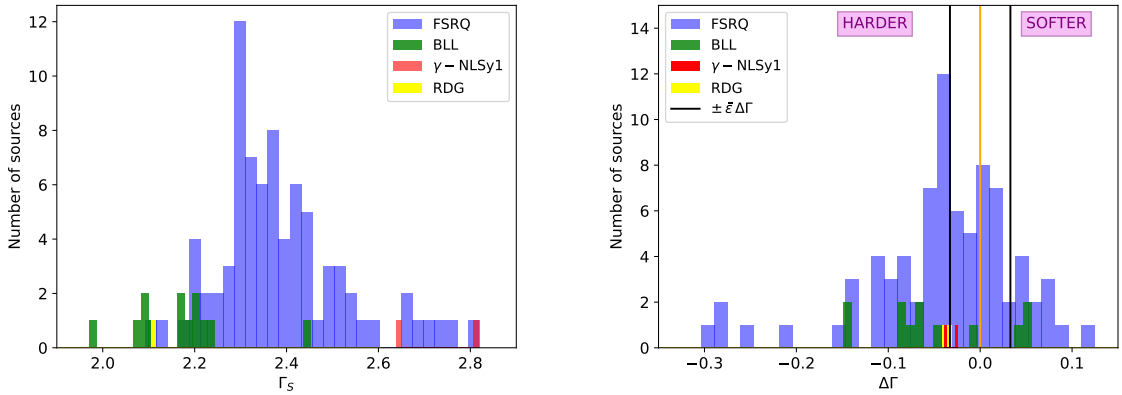

Figure 12: *The left panel shows the distribution of the mean photon index for each AGN type. The right panel represents the distribution of the changes in the photon index of the sources during the flaring state, for every type of sources. The orange vertical line delimits from which* $\Delta\Gamma$ *value sources are considered softer based on the hardness definition. Also, two vertical black lines are displayed to indicate* $\pm\,\bar{\varepsilon}\,\Delta\Gamma$ *which is the mean error of the hardness.*

flaring state. FSRQs have $|\Delta\Gamma|$ values (defined in Equation 7) greater than those for BLLs, meaning that they have flaring state Γ values that differ more from the mean Γ of the sources.

Nevertheless, for all types of sources, in general the dispersion in $\Delta\Gamma$ is narrow and centred around 0, indicating that Γ is not expected to vary much during flaring state, as noted when examining the histogram in Figure 10. This aligns with the findings of Abdo, Ackermann, Ajello, et al. 2010, who stated that the photon index is not expected to vary significantly over time for a given source. Note that when this work mentions that a source becomes harder or softer during flares, it strictly means that the $\Delta\Gamma$ value is negative or positive, respectively. However, sources with $\Delta\Gamma$ values very close to 0 could change of classification if the definition in Equation (7) would not include the sum of the errors. Therefore, it is possible that although in this work a source is categorised as becoming harder or softer, in other studies, it may not be as clear or could be inconclusive. To have a numerical measurement of the error around 0 of $\Delta\Gamma$, the mean $\Delta\Gamma$ error was calculated as shown in Equation (8),

$$\bar{\varepsilon}\,\Delta\Gamma = \sqrt{\bar{\varepsilon}^2_{avg_{\Gamma_{\rm fls}}} + \bar{\varepsilon}^2_{avg_{\Gamma_{\rm S}}}} \tag{8}$$

where $\bar{\varepsilon}_{avg_{\Gamma_{\rm fls}}}$ is the mean value of all the errors of $avg_{\Gamma_{\rm fls}}$ and $\bar{\varepsilon}_{avg_{\Gamma_{\rm S}}}$ is the mean value of all the errors of $avg_{\Gamma_{\rm S}}$. The value of this magnitude is 0.033, and it is represented in plus and minus sign as black vertical lines in the right histogram of Figure 12.

The majority of the sources become harder during flaring state, as shown in the right panel of Figure 12. The 'harder when brighter' effect is fulfilled in 33 out of the 41 bright sources (80 %), of which 28 (85 %) are FSRQs, 4 are BLLs, and 1 RDG. Nevertheless, 8 out of the 41 sources are 'softer when brighter' (19 %), 6 of them FSRQs and 2 BLLs. To determine the significance of this for science, it is necessary to examine whether the value of $\Delta\Gamma$ for these sources deviates significantly from the mean $\Delta\Gamma$ error ($\bar{\varepsilon}\,\Delta\Gamma = 0.033$). If it is very close, it would not be truly conclusive. The 8 sources which are 'softer when brighter' would be more interesting to study, as this feature is not expected to happen. They are: 4FGL J1443.9+2501 (PKS 1441+25), 4FGL J0538.8-4405 (PKS 0537-441), 4FGL J1800.6+7828 (S5 1803+784), 4FGL J1146.9+3958 (S4 1144+40), 4FGL J1224.9+2122 (4C +21.35), 4FGL J1229.0+0202 (3C 273), 4FGL J1522.1+3144 (B2 1520+31), 4FGL J1833.6-2103 (PKS 1830-211). The previous numbers

are presented in the first and second row of Table 6 as well as an extra row summarising the breakdown of the bright sources. In this table, it can be observed that, in general, there are more sources that are harder than softer when brighter, which is expected according to Abdo, Ackermann, Ajello, et al. 2010.

	FSRQ	**BLL**	**RDG**	**γ-NLSy1**	**Total**
'Harder when brighter'	28	4	1	0	33
'Softer when brighter'	6	2	0	0	8
Bright AGN type summary	34	6	1	0	41

Table 6: *Summary table of the number of sources of each type of AGN that meet the criteria of being 'harder when brighter' and 'softer when brighter' during flaring state. The last row provides a summary of the total number of bright sources and their breakdown by AGN type.*

Looking at Tables 3, 4, and 5, more than 60 % of the sources that meet to be bright plus one (or more than one) other characteristic are harder when brighter. Therefore, to be harder when brighter is fulfilled regardless of the extra features. In this work, these features are:

1. Having strong flares with high-energy photons in the energy-weighted light curve.
2. Having strong and new flares in the energy light curve that are not in the photon light curve.
3. Having a photon index that linearly varies with the photon flux during a flare.
4. Being sources that cannot be analysed as single-flare sources.
5. The two previous characteristics, 3rd and 4th, at the same time.
6. When forcing a multi-flare source to behave as a single-flare source, the photon index linearly varies with the photon flux.

The physical process that it is believed to be behind this phenomenon is the synchrotron self-Compton process if the particles are accelerated through shocks in the blazar jets (V. Chitnis et al. 2020).

Regarding the length of the flares with added characteristics, it has been observed that the sources with long flares are the ones that most accomplish other features, as shown in Tables 2, 4, and 5. This is reasonable because as commented before almost the middle of the sources have long flares.

Another conclusion from Tables 2 to 5 is that when more restrictions are placed (i.e., more characteristics are fulfilled), in most cases only FSRQs meet these criteria. This is coherent not only statistically, given that most sources are FSRQs (83.33 %), but also due to their inherent characteristics: they are the brightest sources and those with the most wide variability.

4.2 Results on individual sources

The selected sources which require further attention for individual treatment were: the FSRQ 4FGL J2253.9+1609, for being one of the brightest sources in the sample; the FSRQ 4FGL J1427.9-4206, for having the longest flare in the sample; 4FGL J0319.8+4130 for being the only RDG in the sample; and 4FGL J0948.9+0022 and 4FGL J0324.8+3412 for being the only γ-NLSy1s in the sample.

4FGL J2253.9+1609

The FSRQ 4FGL J2253.9+1609, also known as 3C 454.3 (redshift z = 0.859), is a blazar located in the constellation of Pegasus. It has the brightest blazar γ-ray flare recorded, twice as bright as the Vela Pulsar in our Milky Way galaxy[9]. Its light curve in photon flux units obtained in this work is shown in the left panel of Figure 13. For this particular case, the baseline has a very high value because the flares are very bright. Therefore, the 5σ criterion for defining the flares (Equation 3) has been used only with respect to the mean of the points in quiescence (dark blue dotted-dashed line).

Apart from being extremely bright, it has a wide range of flare duration, ranging from 4.6 months (light green flare) to 4.6 years (magenta flare). Furthermore, it is observed a rapid variability in all the flares, which seems to suggest that the γ-ray emitting region is compact. This is in accordance with Isler et al. 2013 and Jorstad et al. 2013.

Comparing with its light curve in energy flux units, the photon flux light curve weighted in energy (see bottom-left panel of Figure 19 in Appendix B), it can be observed that there are high-energy photons at the beginning of the magenta flare, in the blue flare, in the dark green flare, and in a new flare between the light green and dark blue flares. Consequently, the γ-ray emitting region may be outside of the BLR or involve more complex mechanisms.

This is one of the sources that exhibits 'harder when brighter' behaviour during outbursts. Additionally, regarding the photon index fits made in this work, for all the flares except the light green one, a model with flux-dependent spectral index is favoured over a constant spectral index model. In addition, for the orange flare, a flux-dependent spectral index model is favoured over the global flare. Thus, in this case, the source cannot be treated a singe-flare source. In addition, the global flare fits $\Gamma = \mathrm{m}\cdot\mathrm{Flux} + \mathrm{n}$ and $\Gamma = \mathrm{n}$ are statistically indistinguishable.

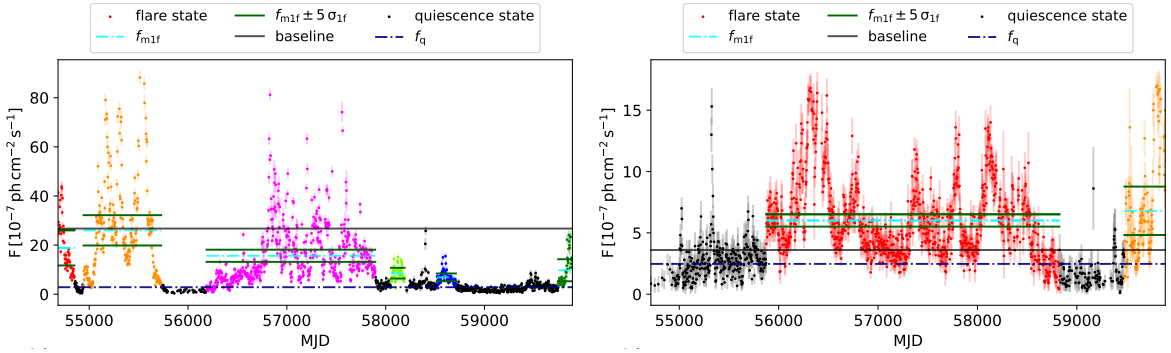

Figure 13: *Light Curve in photon flux units of two FSRQs: 4FGL J2253.9+1609 (left panel) and 4FGL J1427.9-4206 (right panel). The colour points represent the several flares of the source and the black ones the quiescence state. Regarding the colour lines, the mean flux value of the flares is shown in cyan, this mean $\pm 5\,\sigma$ in green, the baseline in grey, and the mean of the points in quiescence in blue.*

4FGL J1427.9-4206

The FSRQ 4FGL J1427.9-4206, also known as PKS 1424-41, has a very strong flare and it lasts for 56 % of the total light curve duration, which correspond to 7.8 years (see right panel of Figure 13). The structure of the flare is very complex, having several flux increases throughout the time. The source reached its maximum emission state in January 2013 (at $\sim$56300 MJD), which was reported by F. D'Ammando et al. 2013, in The Astronomer's Telegram (ATel). Additionally, it is currently in a flaring state, as also

[9] https://www.nasa.gov/science-research/fermi-sees-brightest-ever-blazar-flare/.

reported by Bartolini 2024 in ATel. This source also exhibits the 'harder when brighter' phenomenon, and in both flares, a model where the spectral index depends linearly with the flux is preferred over a model with a constant spectral index. For the longest one, a flux-dependent spectral index model is favoured over the global flare, so in this case, the source neither can be treated a singe-flare source. Furthermore, for the global flare, the flux-dependent spectral index model is statistically significant.

4FGL J0319.8+4130

The bright radio galaxy 4FGL J0319.8+4130 (also known as NGC 1275 and 3C 84) is a powerful radio source located at the centre of the Perseus cluster, at redshift z = 0.01756. NGC 1275 stands out as the brightest radio galaxy detected with *Fermi*-LAT, which observations also revealed flux variability on a weekly time scale (V. Chitnis et al. 2020). Its light curve can be seen in the left panel of Figure 14. In particular, in this work the duration of the flares is short for the red one (6.9 months), medium for the orange and the magenta ones (13 and 18 months, respectively), and large for light green one (1.95 years).

Besides, it was found that this source satisfies the 'harder when brighter' effect. However, this does not coincide with the results of V. Chitnis et al. 2020, who found a significantly 'softer when brighter' trend for this source. The photon index vs. time plot for this source is shown in the right panel of Figure 14, where it is observed that the avg_{Γ_S} and $avg_{\Gamma_{fls}}$ values are very close, meaning a $\Delta\Gamma$ of -0.04. This value is very close to $-\bar{\varepsilon}\,\Delta\Gamma = -0.033$ (see right panel of Figure 12), suggesting that the result is not significantly different from the V. Chitnis et al. 2020 findings (having a $\Delta\Gamma = \pm 0.033$ could change the source to 'softer when brighter' depending of the definition of softer/harder). To have a better comprehension of what is happening here, it would be necessary to study further the source, for example in other wavelengths.

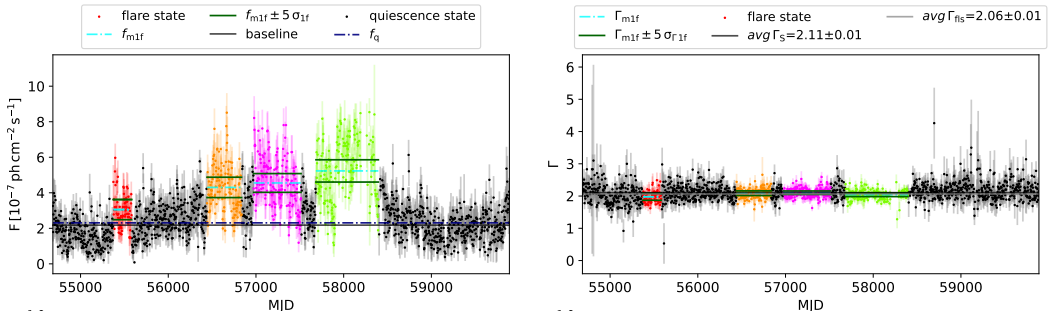

Figure 14: *Light Curve in photon flux units (left panel) and photon index vs. time plot (right panel) of the RDG 4FGL J0319.8+4130. The colour points represent the several flares of the source and the black ones the quiescence state. The mean flux and mean spectral index (in cyan) and these means ± 5 σ (in green) are represented for the y variable. In addition, the baseline in grey and the mean of the points in quiescence in blue are shown in the light curve plot. For the case of the latest plot, the source mean Γ (avg_{Γ_S}) and the average photon index of the global flare mask ($avg_{\Gamma_{fls}}$) are shown as a black and grey line, respectively.*

4FGL J0948.9+0022 & 4FGL J0324.8+3412

To conclude, the cases of γ-NLSy1s are discussed: 4FGL J0948.9+0022 and 4FGL J0324.8+3412, also known as PMN J0948+0022 and 1H 0323+342, respectively. As shown in Figure 15, these sources are not as bright or have as well-defined flares as in the previous cases. However, some studies like Filippo D'Ammando 2019 suggest that the fact that this type of sources exhibit variability and spectral properties in gamma rays indicates that they behave like blazars, so it is important to study them in detail to understand their nature. A good way to do this would be with Cherenkov Telescopes, as shown in the study by Romano et al. 2018. In these cases, the flares are of short duration as defined in this study.

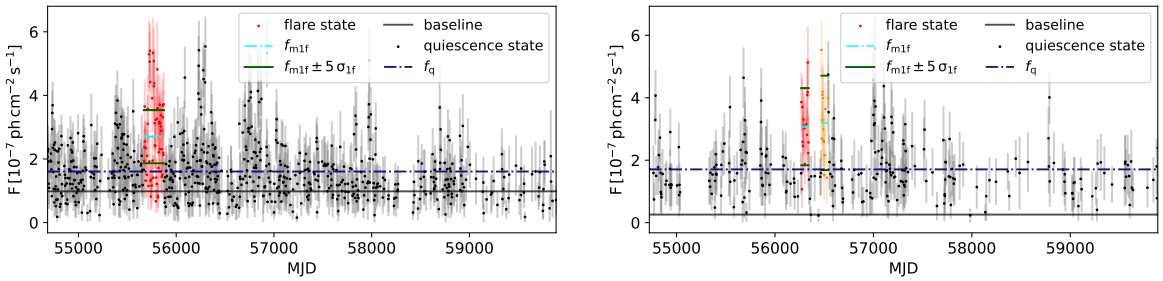

Figure 15: *Light Curve in photon flux units of the γ-NLSy1s 4FGL J0948.9+0022 (left panel) and 4FGL J0324.8+3412 (right panel). The colour points represent the several flares of the source and the black ones the quiescence state. The flare mean flux (in cyan) and this mean ± 5 σ (in green) are represented in the y variable. In addition, the baseline in grey and the mean of the points in quiescence in blue are shown in both plots.*

5 Conclusions

This study has addressed several significant objectives related to the temporal and spectral analysis of AGN gamma rays. The light curve data, ranging from 0.1 to 100 GeV, were obtained from *Fermi*-LAT Light Curve Repository. Other γ-ray properties of the same sources were available in the 4FGL-DR2 catalogue. Below, it is evaluated whether the project objectives have been achieved; summarise the main results and discussions; explore the scientific utility of the project; and offer suggestions for future research directions.

The established objectives have been successfully met. A comprehensive temporal analysis of light curves from a sample of 96 AGN sources spanning a 14-year period was conducted. Furthermore, the relationship between AGN types in terms of their spectral index and behaviour during flares was studied. This study encompassed sources exhibiting both single and multiple flares, providing a comprehensive insight into γ-ray emission behaviours under varying luminosity conditions and flare durations.

Next, a summary of results and discussion is provided.

- **Flare length:** short flares (until 8.2 months) and medium flares (between 8.2 months to 1.7 years) can help constrain the physical parameters of the γ-ray emission zones. Whereas long flares may give information about the jet precession or the accretion flow. 46 sources exhibited at least one long flare, 31 had at least one short flare, and 12 sources showed both long and short flares. These 12 sources, representing 12.5% of the total and 21.82% of the multi-flare sources, are the most varying. This variability in flare duration suggests the presence of complex emission regions and mechanisms. Different regions and processes within the AGN jets could be responsible for flares of different durations in the same source.
- **Bright Sources:** 41 out of 96 sources (42.70%) were found to be bright, with most of them including long flares (29 sources) and some with short flares (13 sources). This suggests that bright sources are often associated with sustained periods of heightened activity, likely due to continuous energy injection into the jets, which is characteristic of powerful AGNs like blazars.

Related to the energy and photon light curves, in 20 out of 96 sources, high flux values on the energy-weighted light curve were observed. This can indicate two distinct physical scenarios:

- **High-Energy Emission Outside the BLR:** flares present in both light curves with high-energy photons suggest that for FSRQs, the emission zone is outside the Broad Line Region, allowing

high-energy photons to escape without being absorbed. For any AGN, this feature implies that the γ-ray emission mechanism is highly efficient, as despite the small number of high-energy photons, the total photon count is sufficient to detect an outburst in the photon flux light curve.

- **Spectral Hardening:** flares appearing in the energy light curve but not in the photon light curve could be due to spectral hardening, where the spectral index decreases, shifting the emission to higher energies.

Investigating sources with these characteristics, especially the brightest ones, is of significant interest for Cherenkov telescopes, as they provide opportunities to gain deeper insights into the high-energy photons received.

Regarding the photon index analysis:

- For 45 out of 204 flares (18.75%) in 35 sources, a flux-dependent spectral index model was favoured over a constant spectral index model. This feature indicates that during flaring states, the photon index linearly varies with the flux, which may be a sign of dynamic changes in the emission processes within the jet, possibly due to variations in the particle acceleration efficiency or changes in the magnetic field strength. This model is not very useful in explaining the data, not only because it is true for only almost 19 % of the flares, but also because, as shown in Figure 10, in most of the flares the photon index remains relatively constant.

- For multi-flare sources, a statistically significant linear fit of the photon index with flux over the global flare was found in 20 out of 163 flares (12.27%) from 17 sources. This suggests that these sources cannot be treated as single-flare sources due to the complex behaviour of their photon index during flares.

- Only 7 flares (4.29%) from 7 sources satisfied both conditions of statistical significance for a linear fit over both a constant index model and the global flare. This indicates that for these sources, the photon index varies linearly with the photon flux during flares, which could imply specific physical conditions or processes within the jet that govern this behaviour.

- In the global flare fit, a flux-dependent spectral index model was favoured in 8 out of 55 multi-flare sources (14.55%) over a constant index model. This means that when forcing the source to behave as a single-flare source, the photon index linearly varies with the photon flux. This result, which is rather unfavourable, leads to the conclusion that it is not a model that explains the reality of the data, i.e. the multi-flare sources cannot be analysed as if they had a single flare.

- The mean photon index is higher for FSRQs than for BLLs, implying that FSRQs are softer and their second peak of the SED is at a lower energy compared to BLLs. This is because FSRQs, being brighter, are observed at greater distances (higher redshift), and thus, the peak is seen at lower energies.

- The hardness of the sources during flaring states showed that FSRQs have greater $|\Delta\Gamma|$ values compared to BLLs, meaning FSRQs experience more significant changes in their photon index during flares. However, the overall dispersion in $\Delta\Gamma$ is narrow and centred around 0, indicating that the photon index does not vary significantly during flares for most sources, aligning with previous findings (Abdo, Ackermann, Ajello, et al. 2010).

- The 'harder when brighter' effect was observed in 33 out of 41 bright sources (80%), with 28 being FSRQs, 4 BLLs, and 1 RDG. This phenomenon supports the synchrotron self-Compton process, where increased brightness correlates with a harder spectrum due to more efficient particle

acceleration and higher energy photon production. Eight sources exhibited the 'softer when brighter' effect, which is not typically expected and justifies further study to understand the underlying mechanisms.

For the case of specific sources analysis:

- **3C 454.3:** this source exhibited a wide range of flare durations (4.6 months to 4.6 years) and rapid variability, suggesting a small γ-ray emission region. The 'harder when brighter' behaviour and favoured flux-dependent spectral index model indicate efficient particle acceleration and synchrotron self-Compton processes.
- **PKS 1424-41:** this source has a very long flare lasting 7.8 years and it is now in flaring state. The 'harder when brighter' phenomenon and favoured flux-dependent spectral index model support the idea of shocks in the jet accelerating particles efficiently.
- **NGC 1275:** this bright radio galaxy showed varying flare durations and a 'harder when brighter' trend. However, discrepancies with previous studies suggesting a 'softer when brighter' trend highlight the need for multi-wavelength analysis to fully understand the emission processes.
- **PMN J0948+0022 and 1H 0323+342:** these sources exhibit variability and spectral properties similar to blazars, suggesting they behave like blazars despite being less bright. Detailed studies using instruments like Cherenkov telescopes are crucial for understanding their nature.

This project has made significant contributions to the field of high-energy astrophysics in several key ways:

- **New method for flare definition:** the introduction of a statistical method to define flares based on the average flux during periods of increased flux and in the Bayesian Block analysis, provides a robust and comparative tool for future studies.
- **Analysis of a large source sample:** an extensive sample of 96 AGN sources was analysed, providing a comprehensive view of flare properties across a γ-ray energy range of 0.1 to 100 GeV. This is significant because the analysis encompasses a large number of sources, ensuring that the results are robust and broadly applicable.
- **Interpretation with updated data:** the use of the LCR facilitated access to updated data and enabled more precise interpretations of individual source light curves. This approach provides an updated view of temporal and spectral variability in AGN sources, crucial for refining theoretical and comparative models in the field.

For future research, considerations for improvement and expansion include:

- **Utilising 4FGL-DR4:** upgrading to the 4FGL-DR4 catalogue would provide access to more recent and comprehensive data, enhancing the precision of analyses and enabling more detailed longitudinal studies.
- **Exploring other spectral models:** in addition to the power-law model, exploring models such as the logarithmic parabola or power-law with an exponential cutoff could offer a more comprehensive view of emission mechanisms during flares.
- **Multi-wavelength research:** integrating data from different wavelengths, could provide a holistic view of the physical processes involved in AGN emissions. This could reveal crucial information about the emission zone location within the jet of AGNs, identifying orphan flares (observed in a

single energy range) and multi-wavelength flares across different spectra (Wang et al. 2022). Additionally, this approach would explore the relationship between variations in different wavelengths and enhance our understanding of the physics behind observed flares.

- **Using data bins shorter than 3 days:** using shorter bins to obtain more precise information about the sources and to define flare durations (exploring other methods) and variability.

In summary, these results provide significant insights into the temporal and spectral behaviours of AGN, emphasising the importance of innovative methods and updated data and the need for detailed multi-wavelength analysis to advance our understanding of these powerful cosmic sources and their γ-ray emissions. The methods developed for flare identification and characterisation in this study offer a robust framework for future research, enhancing the comparability and understanding of AGN variability and emission mechanisms.

Acknowledgements

This research has made use of the LCR data. Therefore, special acknowledgment is given to Daniel Kocevski, who is currently maintaining the LCR, with additional support from Janeth Valverde, Simone Garrappa, Michela Negro, Jean Ballet, and Benoit Lott, on behalf of NASA and the Fermi Large Area Telescope Collaboration. Additionally, the *Fermi*-LAT Collaboration is acknowledged. This research collaboration, whose article contributions are attributed to its participating partner institutions and agencies, has supported both the development and operation of the LAT as well as scientific data analysis. Without their efforts, there would not have been any *Fermi*-LAT catalogue, such as the 4FGL (and its different data releases) used in this work.

References

Abdo, A. A., M. Ackermann, I. Agudo, et al. (June 2010). "The Spectral Energy Distribution of Fermi Bright Blazars". In: *ApJ* 716.1, pp. 30–70. DOI: 10.1088/0004-637X/716/1/30.

Abdo, A. A., M. Ackermann, M. Ajello, et al. (Feb. 2010). "Spectral Properties of Bright Fermi-Detected Blazars in the Gamma-Ray Band". In: *ApJ* 710.2, pp. 1271–1285. DOI: 10.1088/0004-637X/710/2/1271.

Abdollahi, S., F. Acero, M. Ackermann, et al. (Mar. 2020). "Fermi Large Area Telescope Fourth Source Catalog". In: *ApJS* 247.1, 33, p. 33. DOI: 10.3847/1538-4365/ab6bcb.

Abdollahi, S., F. Acero, L. Baldini, et al. (June 2022). "Incremental Fermi Large Area Telescope Fourth Source Catalog". In: *ApJS* 260.2, 53, p. 53. DOI: 10.3847/1538-4365/ac6751.

Abdollahi, S., M. Ajello, et al. (Apr. 2023). "The Fermi-LAT Lightcurve Repository". In: *ApJS* 265.2, p. 31. DOI: 10.3847/1538-4365/acbb6a.

Atwood, W. B. et al. (June 2009). "The Large Area Telescope on the Fermi Gamma-Ray Space Telescope Mission". In: *ApJ* 697.2, pp. 1071–1102. DOI: 10.1088/0004-637X/697/2/1071.

Ballet, J., P. Bruel, et al. (July 2023). "Fermi Large Area Telescope Fourth Source Catalog Data Release 4 (4FGL-DR4)". In: *arXiv e-prints*. DOI: 10.48550/arXiv.2307.12546.

Ballet, J., T. H. Burnett, et al. (May 2020). "Fermi Large Area Telescope Fourth Source Catalog Data Release 2". In: *arXiv e-prints*. DOI: 10.48550/arXiv.2005.11208.

Bartolini, Chiara (Jan. 2024). "Fermi-LAT detection of renewed gamma-ray activity from the FSRQ PKS 1424-41". In: *The Astronomer's Telegram* 16406, p. 1.

Bednarek, W. (June 1997). "Cascade initiated by VHE γ-rays in the radiation field of a close massive companion." In: *A&A* 322, pp. 523–532.

Blandford, R., D. Meier, and A. Readhead (Aug. 2019). "Relativistic Jets from Active Galactic Nuclei". In: *Annual Review of Astronomy and Astrophysics* 57, pp. 467–509. DOI: 10.1146/annurev-astro-081817-051948.

Blandford, R. D. and M. J. Rees (Dec. 1974). "A "twin-exhaust" model for double radio sources." In: *MNRAS* 169, pp. 395–415. DOI: 10.1093/mnras/169.3.395.

Bose, D., V. R. Chitnis, P. Majumdar, and B. S. Acharya (Jan. 2022). "Ground-based gamma-ray astronomy: history and development of techniques". In: *European Physical Journal Special Topics* 231.1, pp. 3–26. DOI: 10.1140/epjs/s11734-021-00396-3.

Bose, D., V. R. Chitnis, P. Majumdar, and A. Shukla (Jan. 2022). "Galactic and extragalactic sources of very high energy gamma rays". In: *European Physical Journal Special Topics* 231.1, pp. 27–66. DOI: 10.1140/epjs/s11734-022-00434-8.

Böttcher, M. (Dec. 2008). "Implications of the VHE γ-Ray Detection of 3C279". In: American Institute of Physics Conference Series 1085, pp. 427–430. DOI: 10.1063/1.3076699.

Chen, X. et al. (May 2013). "Long-term variability of extragalactic radio sources in the Planck Early Release Compact Source Catalogue". In: *A&A* 553, A107. DOI: 10.1051/0004-6361/201220517.

Chitnis, Varsha et al. (Aug. 2020). "X-ray and Gamma-ray Variability of NGC 1275". In: *Galaxies* 8.3, p. 63. DOI: 10.3390/galaxies8030063.

D'Ammando, F. et al. (Jan. 2013). "Detection of a strong optical and gamma-ray flare from blazar PKS 1424-41". In: *The Astronomer's Telegram* 4714, p. 1.

D'Ammando, Filippo (Nov. 2019). "Relativistic Jets in Gamma-Ray-Emitting Narrow-Line Seyfert 1 Galaxies". In: *Galaxies* 7.4, p. 87. DOI: 10.3390/galaxies7040087.

D'Ammando, F. et al. (2013). "Gamma-ray emitting narrow-line Seyfert 1 galaxies. New discoveries and open questions". In: *Proceedings of the International Astronomical Union* 9.S304, pp. 140–143. DOI: 10.1017/S1743921314003561.

Dermer, Charles D. and Govind Menon (2009). *High Energy Radiation from Black Holes: Gamma Rays, Cosmic Rays, and Neutrinos*. Princeton Series in Astrophysics. Princeton University Press. ISBN: 9781400831494.

Gaur, H. et al. (Nov. 2019). "Properties of radio-loud quasars in the Sloan Digital Sky Survey". In: *A&A* 631, A46. DOI: 10.1051/0004-6361/201935398.

Goodrich, Robert W. (July 1989). "Spectropolarimetry of "Narrow-Line" Seyfert 1 Galaxies". In: *ApJ* 342, p. 224. DOI: 10.1086/167586.

Hassan, T. et al. (Jan. 2013). "Gamma-ray active galactic nucleus type through machine-learning algorithms". In: *MNRAS* 1, pp. 220–225. DOI: 10.1093/mnras/sts022.

Hillas, A. M. (Aug. 1985). "Cerenkov Light Images of EAS Produced by Primary Gamma Rays and by Nuclei". In: *19th International Cosmic Ray Conference (ICRC19), Volume 3*, p. 445.

Hovatta, Talvikki and Elina Lindfors (Dec. 2019). "Relativistic Jets of Blazars". In: *New Astronomy Reviews* 87, p. 101541. DOI: 10.1016/j.newar.2020.101541.

Impiombato, D. et al. (Jan. 2011). "Optical and Infrared Photometry of the Blazar PKS 0537-441: Long and Short Timescale Variability". In: *ApJS* 192.1, p. 12. DOI: 10.1088/0067-0049/192/1/12.

Isler, Jedidah C. et al. (Dec. 2013). "A Time-resolved Study of the Broad-line Region in Blazar 3C 454.3". In: *ApJ* 779.2, 100, p. 100. DOI: 10.1088/0004-637X/779/2/100.

Jorstad, Svetlana G. et al. (Aug. 2013). "A Tight Connection between Gamma-Ray Outbursts and Parsec-scale Jet Activity in the Quasar 3C 454.3". In: *ApJ* 773.2, p. 147. DOI: 10.1088/0004-637X/773/2/147.

Kellermann, Kenneth I. and Frazer N. Owen (1988). "Radio galaxies and quasars." In: *Galactic and Extragalactic Radio Astronomy*, pp. 563–602.

Mücke, A. et al. (Mar. 2003). "BL Lac objects in the synchrotron proton blazar model". In: *Astroparticle Physics* 18.6, pp. 593–613. DOI: 10.1016/S0927-6505(02)00185-8.

Nalewajko, Krzysztof (Apr. 2013). "The brightest gamma-ray flares of blazars". In: *MNRAS* 430.2, pp. 1324–1333. DOI: 10.1093/mnras/sts711.

Nalewajko K., Mitchell C. and M. Sikora (June 2014). "Constraining the Location of Gamma-Ray Flares in Luminous Blazars". In: *ApJ* 789.2, p. 161. DOI: 10.1088/0004-637x/789/2/161.

Neyman, J. and E. S. Pearson (Dec. 1928). "On the use and interpretation of certain test criteria for purposes of statistical inference". In: *Biometrika* 20A.3-4, pp. 263–294. DOI: 10.1093/biomet/20A.3-4.263.

Osterbrock, D. E. and R. W. Pogge (Oct. 1985). "The spectra of narrow-line Seyfert 1 galaxies." In: *ApJ* 297, pp. 166–176. DOI: 10.1086/163513.

Ostorero, L., M. Villata, and C. M. Raiteri (June 2004). "Helical jets in blazars. Interpretation of the multifrequency long-term variability of AO 0235+16". In: *A&A* 419, pp. 913–925. DOI: 10.1051/0004-6361:20035813.

Padovani, P. et al. (Aug. 2017). "Active galactic nuclei: what's in a name?" In: *The Astronomy and Astrophysics Review* 25.1, p. 2. DOI: 10.1007/s00159-017-0102-9.

Paliya, Vaidehi S. et al. (Feb. 2019). "General Physical Properties of Gamma-Ray-emitting Narrow-line Seyfert 1 Galaxies". In: *ApJ* 872.2, p. 169. DOI: 10.3847/1538-4357/ab01ce.

Principe, G et al. (Aug. 2021). "Gamma-ray emission from young radio galaxies and quasars". In: *Monthly Notices of the Royal Astronomical Society* 507.3, pp. 4564–4583. DOI: 10.1093/mnras/stab2357.

Rani, B. et al. (Sept. 2013). "Constraining the location of rapid gamma-ray flares in the flat spectrum radio quasar 3C 273". In: *A&A* 557, A71. DOI: 10.1051/0004-6361/201321440.

Resconi, E. et al. (Aug. 2009). "The classification of flaring states of blazars". In: *A&A* 502.2, pp. 499–504. DOI: 10.1051/0004-6361/200911770.

Romano, P. et al. (Dec. 2018). "Prospects for gamma-ray observations of narrow-line Seyfert 1 galaxies with the Cherenkov Telescope Array". In: *MNRAS* 481.4, pp. 5046–5061. DOI: 10.1093/mnras/sty2484.

Scargle, Jeffrey D. et al. (Feb. 2013). "Studies in Astronomical Time Series Analysis. VI. Bayesian Block Representations". In: *ApJ* 764.2, p. 167. DOI: 10.1088/0004-637X/764/2/167.

Shukla, A. et al. (Feb. 2018). "Short-timescale γ-Ray Variability in CTA 102". In: *ApJL* 854.2, p. L26. DOI: 10.3847/2041-8213/aaacca.

Sikora, Marek, Mitchell C. Begelman, and Martin J. Rees (Jan. 1994). "Comptonization of Diffuse Ambient Radiation by a Relativistic Jet: The Source of Gamma Rays from Blazars?" In: *ApJ* 421, p. 153. DOI: 10.1086/173633.

Stickel, M. et al. (June 1991). "The Complete Sample of 1 Jansky BL Lacertae Objects. I. Summary Properties". In: *ApJ* 374, p. 431. DOI: 10.1086/170133.

Tchekhovskoy, Alexander, Ramesh Narayan, and Jonathan C. McKinney (2011). "Efficient Generation of Jets from Magnetically Arrested Accretion on a Rapidly Spinning Black Hole". In: *Mon. Not. Roy. Astron. Soc.* 418, pp. L79–83. DOI: 10.1111/j.1745-3933.2011.01147.x.

Urry, C. Megan and Paolo Padovani (Sept. 1995). "Unified Schemes for Radio-Loud Active Galactic Nuclei". In: *Publications of the Astronomical Society of the Pacific* 107, p. 803. DOI: 10.1086/133630.

Van den Berg, Jacobus P. et al. (Mar. 2019). "Systematic Physical Characterization of the γ-Ray Spectra of 2FHL Blazars". In: *ApJ* 874.1, p. 47. DOI: 10.3847/1538-4357/aafdfd.

Wagner, S. J. and A. Witzel (Jan. 1995). "Intraday Variability In Quasars and BL Lac Objects". In: *Annual Review of Astronomy and Astrophysics* 33, pp. 163–198. DOI: 10.1146/annurev.aa.33.090195.001115.

Wang, Ze-Rui et al. (Jan. 2022). "Unified model for orphan and multiwavelength blazar flares". In: *Physical Review D* 105.2, p. 023005. DOI: 10.1103/PhysRevD.105.023005.

Yoshida, Kenji et al. (Sept. 2023). "Flare Duty Cycle of Gamma-Ray Blazars and Implications for High-energy Neutrino Emission". In: *ApJ* 954.2, p. 194. DOI: 10.3847/1538-4357/acea74.

A Appendix: Table of definitions

Below is Table A, which compiles all the abbreviations used in the report and their respective definitions. These abbreviations can be acronyms, symbols, or definitions that appear in the text or in equations. They are sorted alphabetically appearing first numbers. For the symbols, the first letter of the name is used to sort them (for example: Δ is pronounced as Delta, so D is the letter used to sort the symbol).

Abbreviation	**Definition**
4FGL-DR2	Fourth Fermi Gamma-ray LAT catalogue for Data Release 2.
AGN	Active Galactic Nucleus. Brightest central region of a type of galaxy known as Active Galaxies, characterised by exceptionally luminous centres within a very concentrated volume fuelled by the process of accretion onto supermassive black holes.
$avg_{\Gamma_{\rm fls}}$	Average photon index of the flares. Obtained by using the global flare mask to average the photon index of all these points. It appears in Equation (7).
$avg_{\Gamma_{\rm S}}$	Source average photon index, obtained from the catalogue 4FGL-DR2. It appears in Equation (7).
BLL	BL Lacertae objects. Type of blazar characterised by having optical emission lines with an equivalent width below 5Å or lack these lines entirely.
bsl	Baseline. Background flux level in the light curve of an AGN.
BB	Bayesian Block. Algorithm described by Scargle et al. 2013. In this work is used to define a flare based on the detection of significant changes in photon flux compared to previous bins using data blocks.
BLR	Broad Line Region. Rapidly moving gas clouds that may be located around the accretion disk in an AGN.
Condition 1	Linear fit $\Gamma = \mathrm{m}\cdot\mathrm{Flux} + \mathrm{n}$ is statistically preferred over $\Gamma = \mathrm{n}$ for an AGN flare, implying that during the flare the photon index linearly depends on the photon flux. It appears in Table 4.
Condition 2	Linear fit $\Gamma = \mathrm{m}\cdot\mathrm{Flux} + \mathrm{n}$ is statistically significant over the global flare fit for flares of multi-flare sources. These sources cannot be analysed as if they were single-flare sources because they have at least one flare significant over the global flare. It appears in Table 5.
Condition 3	Statistically significance of the fit $\Gamma = \mathrm{m}\cdot\mathrm{Flux} + \mathrm{n}$ over both $\Gamma = \mathrm{n}$, and the global flare fit for flares of multi-flare sources. Implying the same as condition 1 and 2 together for the same flare. It appears in Table 5.
Condition 4	For the global flare (multi-flare sources), the linear fit $\Gamma = \mathrm{m}\cdot\mathrm{Flux} + \mathrm{n}$ is better than $\Gamma = \mathrm{n}$. This means that when forcing the source to behave as a single-flare source, the photon index linearly varies with the photon flux. It appears in Table 5.
$\Delta\,\Gamma$	Average variation of photon index. Defined in Equation (7).
E_0	Pivot energy. Pivot Energy is a reference energy chosen to coincide with the energy level where the relative uncertainty on the differential flux reaches its lowest point. It appears in Equation (2) and (4).
EC	External Compton. Leptonic model for explaining the second SED peak of a flat spectrum radio quasar in which inverse compton interactions occur between the same population of accelerated electrons producing synchrotron in the jet and either the photons produced by Synchrotron self-Compton or external photons from other parts of the AGN.
$\varepsilon_{avg_{\Gamma_{\rm S}}}$	Error of $avg_{\Gamma_{\rm S}}$. It appears in Equation (7).

$\varepsilon_{avg_{\Gamma_{\rm fls}}}$	Error of $avg_{\Gamma_{\rm fls}}$. It appears in Equation (7).
$\varepsilon_{m_{\rm 1f(n=ct)}}$	Error of $m_{\rm 1f(n=ct)}$. It appears in Equation (6).
$\varepsilon_{m_{\rm global}}$	Error of $m_{\rm global}$. It appears in Equation (6).
$\varepsilon_{\rm bsl}$	Error of the baseline. It appears in Equation (3).
$\varepsilon_{f_{\rm q}}$	Error of the mean flux of the points in quiescence. It appears in Equation (6).
$\bar{\varepsilon}_{avg_{\Gamma_{\rm fls}}}$	Mean average photon index of the flares. Mean value of all the errors of $avg_{\Gamma_{\rm fls}}$. It appears in Equation (8).
$\bar{\varepsilon}_{avg_{\Gamma_{\rm S}}}$	Mean sources average photon index. Mean value of all the errors of $avg_{\Gamma_{\rm S}}$. It appears in Equation (8).
$\bar{\varepsilon}\,\Delta\Gamma$	Mean $\Delta\Gamma$ error. Defined in Equation (8).
Fermi	Fermi Gamma-ray Space Telescope. NASA's space observatory that detects gamma rays in order to study the most energetic sky.
FSRQ	Flat Spectrum Radio Quasar. Type of blazar characterised by having optical emission lines with an equivalent width greater than 5Å. Also, it is a core-dominated radio-loud quasar.
$f_{\rm m1f}$	Mean flux of the points that define a flare.
$f_{\rm q}$	Mean flux of the points in quiescence state (out of flare state).
GBM	Gamma-ray Burst Monitor. Instrument on the *Fermi* mission which detects X-rays and gamma rays within the 8 keV to 40 MeV energy range.
γ-NLSy1	γ-ray emission NLSy1 galaxy.
Γ	Spectral index of the power-law assumed to has an AGN in the second SED hump in energies of gamma rays.
H	Harder. When a source becomes harder when brighter during flaring state.
HBL	High-frequency peaked BL Lacertae object.
HSP	High-frequency Peaked Source, in which $\log \nu_{\rm peak} > 15$ for the first peak of the blazars SED.
IACT	Imaging Atmospheric Cherenkov Telescope. Ground-based telescope which is capable of detect Cherenkov radiation.
IC scattering	Inverse Compton scattering. γ-ray emission process in which a γ-ray photon is emitted when a low-energy photon collides with an ultra-relativistic electron, transferring energy to the photon.
IBL	Intermediate-frequency peaked BL Lacertae object.
ISP	Intermediate-frequency peaked source in which $14 < \log \nu_{\rm peak} < 15$ for the first peak of the blazars SED.
LAT	Large Area Telescope. Primary instrument on the Fermi mission. It is an imaging high-energy γ-ray telescope, sensitive to photons with energies between 20 MeV to 300 GeV.
LC	Light curve. Plot representing the received photon flux over time.
LCR	Fermi LAT Light Curve Repository. Database of light curves of sources observed by *Fermi*-LAT.
LBL	Low-frequency peaked BL Lacertae object.
LSP	Low-frequency peaked source in which $\log \nu_{\rm peak} < 14$ for the first peak of the blazars SED.
$m_{\rm 1f(n=ct)}$	m value of the fit $\mathrm{y} = \mathrm{m\,x} + \mathrm{ct}$ for AGN flares, where m is the slope and ct is a constant. It appears in Equation (6).
$m_{\rm global}$	m value of the fit $\mathrm{y} = \mathrm{m\,x} + \mathrm{n}$ for an AGN global flare. It appears in Equation (6).
N	Received photon flux in units of $\mathrm{ph\,cm^{-2}\,s^{-1}}$ in Equation (2).

N_0	Photon flux density (photon flux per energy). It appears in Equation (2).
NLR	Narrow Line Region. Gas clouds located in the outermost regions of the AGN.
NLSy1	Narrow-line Seyfert 1. Seyfert 1 galaxy which display broad permitted lines with small widths.
RDG	Radio galaxy. Misaligned AGN which have jet inclination angles of 10°.
S	Softer. When a source becomes softer when brighter during flaring state.
σ_{1f}	Mean flux error for a flare. Error of f_{m1f}.
SSC	Synchrotron self-Compton. Leptonic model for explaining the second SED peak of a BLL in which electrons accelerated in the jet generate observed emissions through IC scattering involving photons emitted as synchrotron radiation within the jet.
SSRQ	Steep-spectrum radio quasar. Lobe-dominated radio-loud quasar.
TS	Test statistic. Distributed as χ^2 to assess the significance of a source above the expected background.
VHE	Very High Energy. In the context of high-energy astrophysics are energies above 100 GeV.
VI	Variability index. Serves as an indicator of the average fractional variability with dF/F measured over yearly timescales for AGNs.

Table A: *Table of definitions. It compiles all the abbreviations used in the report and their respective definitions.*

B Appendix: Light Curves of sources with flares in their Energy Light Curves

Here, the light curves of 8 sources are presented. Each source has two light curves: one in photon flux units and the other in energy flux units, with the latter being the photon flux light curve weighted by energy. These sources exhibit flares in their energy light curves that do not appear in the photon light curve. Additionally, in some of the outburst common to both light curves, the energy light curve shows high-energy photons.

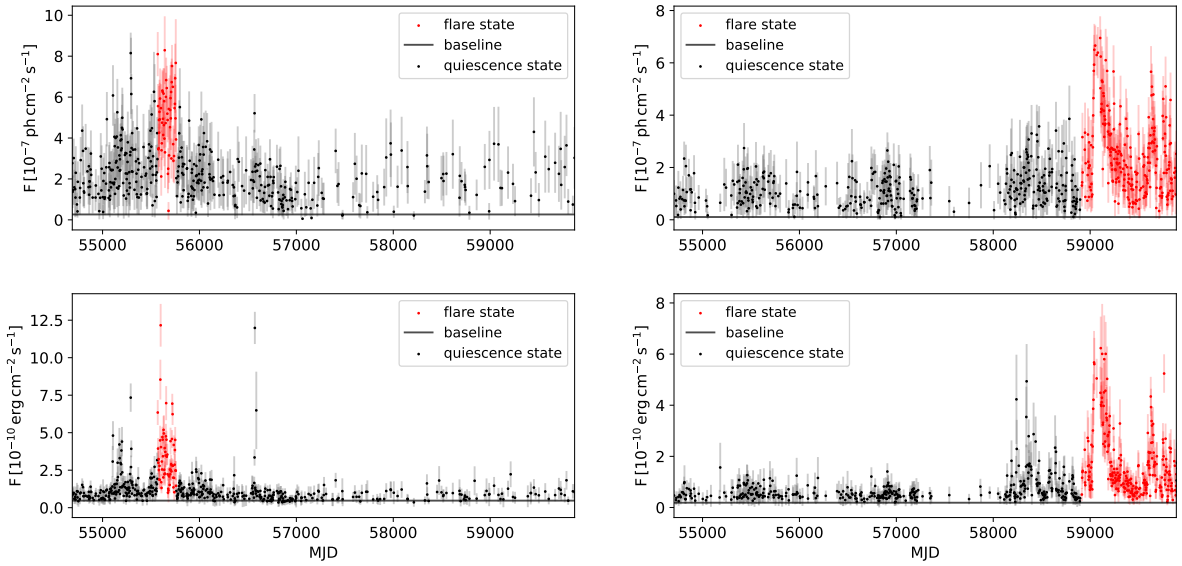

Figure 16: *Light Curve in photon flux units (upper panels) and in energy flux units (bottom panels) of the FSRQ 4FGL J1625.7-2527 (left) and 4FGL J1408.9-0751 (right). The red points represent the flare identified in this work and the black ones the quiescence state. The baseline is represented as a grey continuous line. In the energy light curves, the new flares not present at the photon light curve are located at MJD ∼ 56585 for the left source and at MJD ∼ 58351 for the right source.*

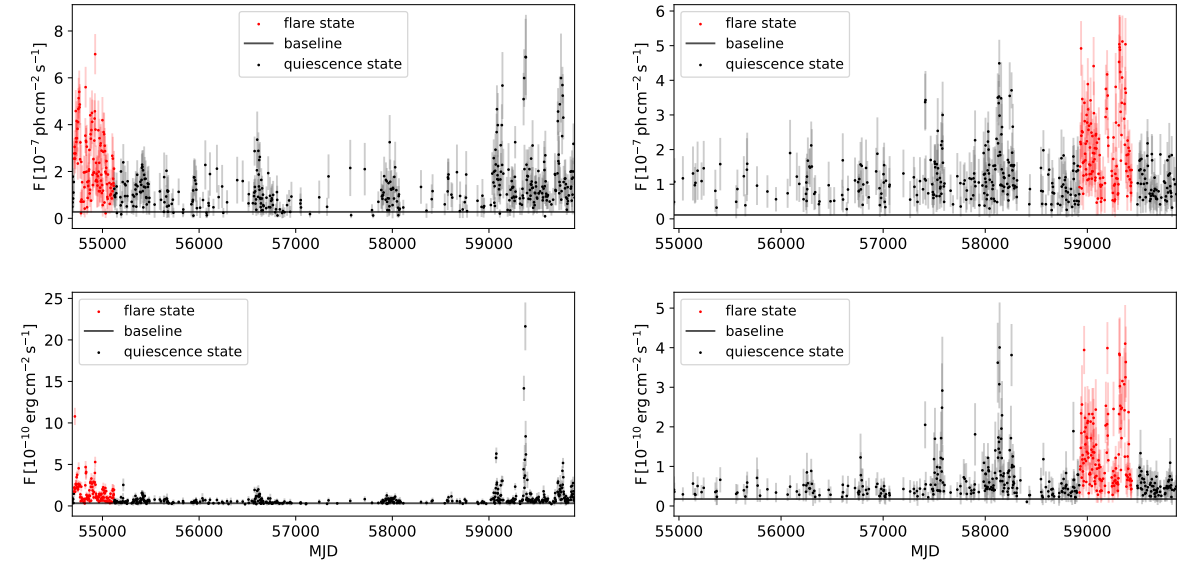

Figure 17: *Light Curve in photon flux units (upper panels) and in energy flux units (bottom panels) of the FSRQ 4FGL J1457.4-3539 (left) and 4FGL J0515.6-4556 (right). The red points represent the flare identified in this work and the black ones the quiescence state. The baseline is represented as a grey continuous line. In the energy light curves, the new flares not present at the photon light curve are located at MJD ∼ 59376 for the left source and at MJD ∼ 57579 and 58142 for the right source.*

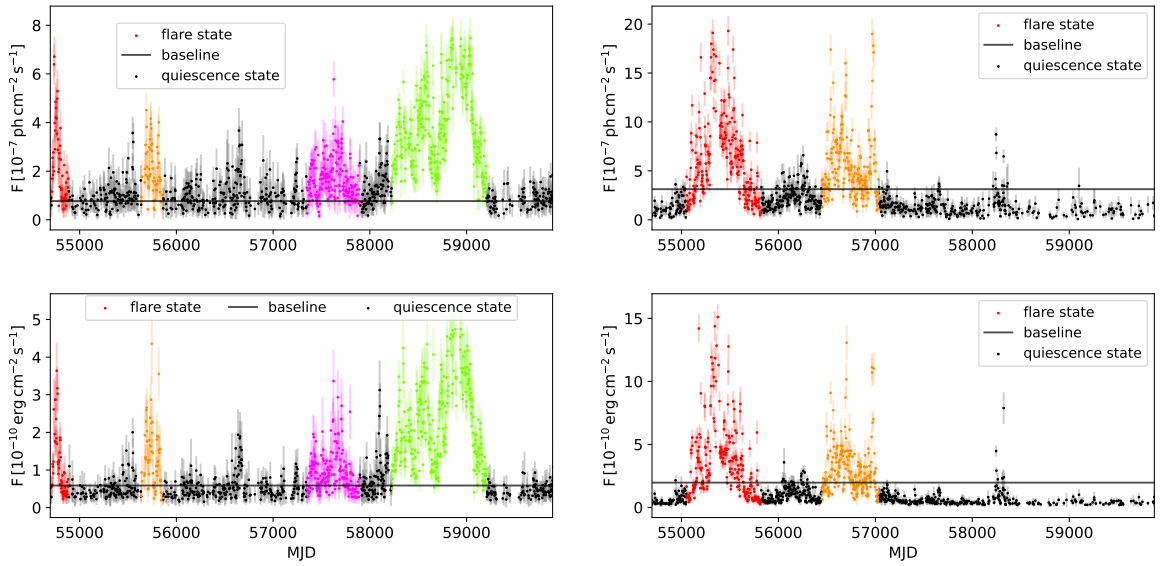

Figure 18: *Light Curve in photon flux units (upper panels) and in energy flux units (bottom panels) of the FSRQ 4FGL J0210.7-5101 (left) and 4FGL J1224.9+2122 (right). The colour points represent the flares identified in this work and the black ones the quiescence state. The baseline is represented as a grey continuous line. In the energy light curves, the new flares not present at the photon light curve are located at MJD ∼ 58100 for the left source and at MJD ∼ 58323 for the right source.*

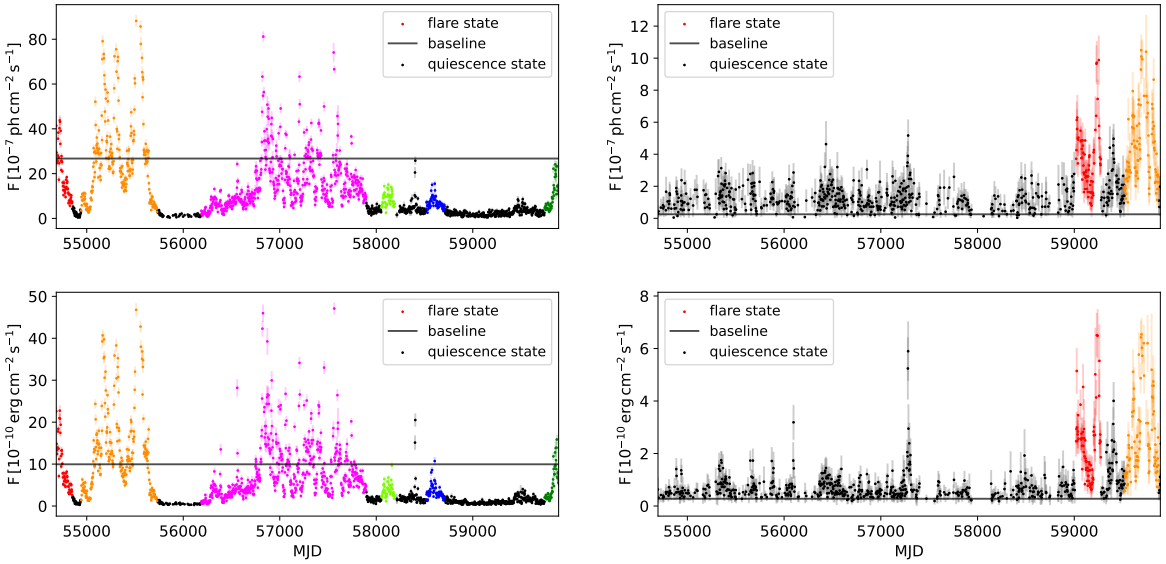

Figure 19: *Light Curve in photon flux units (upper panels) and in energy flux units (bottom panels) of the FSRQ 4FGL J2253.9+1609 (left) and 4FGL J1958.0-3845 (right). The colour points represent the flares identified in this work and the black ones the quiescence state. The baseline is represented as a grey continuous line. In the energy light curves, the new flares not present at the photon light curve are located at MJD ∼ 58400 for the left source and at MJD ∼ 56097 and 57282 for the right source.*